

## Model of $n = 2$ RMP ELM suppression in DIII-D

J D Callen,<sup>1</sup> R Nazikian,<sup>2</sup> C Paz-Soldan,<sup>3</sup> N M Ferraro,<sup>2</sup>  
M T Beidler,<sup>1</sup> C C Hegna<sup>1</sup> and R J La Haye<sup>3</sup>

<sup>1</sup>University of Wisconsin, 1500 Engineering Drive, Madison, WI 53706-1609 USA

<sup>2</sup>Princeton Plasma Physics Laboratory, PO Box 451, Princeton, NJ 08543-0451 USA

<sup>3</sup>General Atomics, PO Box 85608, San Diego, CA 92186-5608 USA

E-mail: [jdcallen@wisc.edu](mailto:jdcallen@wisc.edu), <http://homepages.cae.wisc.edu/~callen>

**Abstract.** Recent DIII-D experiments [Paz-Soldan *et al* 2015 *Phys. Rev. Lett.* **114**, 105001; Nazikian *et al* 2015 *Phys. Rev. Lett.* **114**, 105002] explored effects of resonant magnetic perturbations (RMPs) near the minimum applied  $n = 2$  RMP amplitude needed for suppression of type I edge localized modes (ELMs) in ITER-relevant low collisionality H-mode plasmas. Further data analysis of DIII-D discharge 158115 has focused on the evolution of edge magnetic and plasma responses to ELM crashes, especially the one immediately preceding bifurcation into ELM suppression. A comprehensive model is developed to describe and quantify the key processes involved in the many sequential stages of RMP effects that lead to bifurcation into the ELM-suppressed pedestal state: 1) in the ELMing “equilibrium” before suppression, flow-screening of RMPs is strong and the predicted resonant magnetic perturbations induced at  $q = m/n$  rational surfaces are small; 2) however, these RMP-induced perturbations are large enough for magnetic flutter transport to flatten the electron pressure profiles there, so  $\omega_{\perp e} \rightarrow \omega_E$  at the rational surfaces; 3) the predicted effects of the abrupt, large forced magnetic reconnection induced by an ELM crash correlate well with the observed extra  $n = 2$  tearing-type magnetic response and locking of the plasma to the RMP frame (analogous to field-error-induced mode locking); 4) the ELM crash thereby produces a modest width 8/2 seed magnetic island whose growth is governed by a nonlinear modified Rutherford equation (like in neoclassical tearing modes); 5) then, if the externally imposed 8/2 RMP is large enough, the observed tearing-type response grows slowly and saturates approximately as predicted; and 6) finally, the predicted magnetic-flutter-induced electron transport diffusivities are consistent with those that produce the observed reduction in the  $T_e$  and  $n_e$  gradients at the pedestal top which stabilize P-B modes and thereby suppress ELMs. This new model’s criteria for RMP ELM suppression are similar to previous empirical ones for DIII-D discharge 158115. However, its key physical processes and scalings are quite different: 1) an ELM crash causes abrupt reconnection and bifurcation into a mode-locked state at a rational surface, 2)  $\omega_E \rightarrow 0$  at the 8/2 rational surface is a consequence of an ELM crash not the initiator of ELM suppression, 3) the RMP drive must be large enough to produce island growth in the nonlinear modified Rutherford equation, and 4) electron flow, flutter transport and collisionality effects are complicated and intertwined.

## 1. Introduction

*Suppression of ELMs by RMPs.* Edge localized modes (ELMs) are major concerns for ITER plasmas [1]. Pioneering experiments [2]–[5] in DIII-D have used small, externally applied three-dimensional (3-D) magnetic perturbations that are resonant at the  $q = m/n$  rational surfaces in the edge of H-mode plasmas to stabilize ideal magnetohydrodynamic (MHD) peeling-ballooning (P-B) instabilities [6]–[9] and thereby suppress the most deleterious type I ELMs [10, 11]. The key physical processes responsible for how resonant magnetic perturbations (RMPs) suppress ELMs in tokamak plasmas are not yet understood [12, 13].

*Recent  $n = 2$  DIII-D results.* Seminal experiments in DIII-D [14, 15] explored effects of RMPs near the minimum applied  $n = 2$  amplitude that produced type I ELM suppression in ITER-relevant low collisionality pedestals. Figure 1 shows that when the  $n = 2$  magnetic response measured on the high field side (HFS) is large enough, at about 3.7 and 4.7 s, abrupt bifurcations into ELM suppression occur, as shown by the absence of spikes in  $D_\alpha$  in Fig. 1(c) just after these times. These ELM-suppressed plasma states have: 1) an extra\* (red asterisks indicate parts of figures being discussed) externally measured HFS  $n = 2$  tearing-type poloidal magnetic field response  $|\delta B_\theta|$  [15], 2) increased\* carbon (subscript C) toroidal (subscript t) flow speed  $V_{Ct}$  in the top half of the pedestal [15], and 3) slightly reduced\* pedestal top electron density  $n_{e,\text{ped}}$  and temperature  $T_{e,\text{ped}}$ . Figures 5 and 6 below show the behavior of  $|\delta B_\theta|$  and  $V_{Ct}$  on sequentially shorter time intervals around the time of the ELM crash at 4.7 s that immediately precedes the bifurcation into the ELM-suppressed state.

*Scope of paper.* This paper develops a comprehensive model for describing and quantifying the many sequential stages of the temporal development of the magnetic field and pedestal plasma as type I ELMs are suppressed in the DIII-D discharge 158115 data shown in Figs. 1, 4–7. This novel model for near threshold ELM suppression involves a combination of forced magnetic reconnection (FMR) theory of the two metastable states that occur in tokamaks with externally applied RMPs (sections 2,3,5–8), numerical and analytic modeling of the perturbed fields in the pedestal plasma (section 2), kinetic-based, nonlinear magnetic flutter transport (sections 3,6,7,9), nonlinear magnetic island evolution (section 8) and some phenomenological descriptions. The emphasis is on developing models for all the key physical processes involved in the many stages of ELM-crash-induced suppression of ELMs by RMPs and direct comparisons of these model predictions with measured quantities in DIII-D discharge 158115 [14, 15].

*Outline.* The following sections describe: 2) basics of FMR theory, 3) the strong flow-screening that occurs before bifurcation, 4)  $\delta B_\theta$  and  $V_{Ct}$  responses to an ELM crash, 5) how an ELM crash can produce abrupt RMP penetration and a significant resonant field and seed magnetic island width at the  $q = 8/2$  rational surface, 6) plasma flow evolution into a RMP mode-locked state during an ELM crash, 7) transient effects during the initial tearing response stage, 8) bifurcation into a nonlinear state in which the seed island width initially grows slowly and ultimately saturates at a RMP-induced

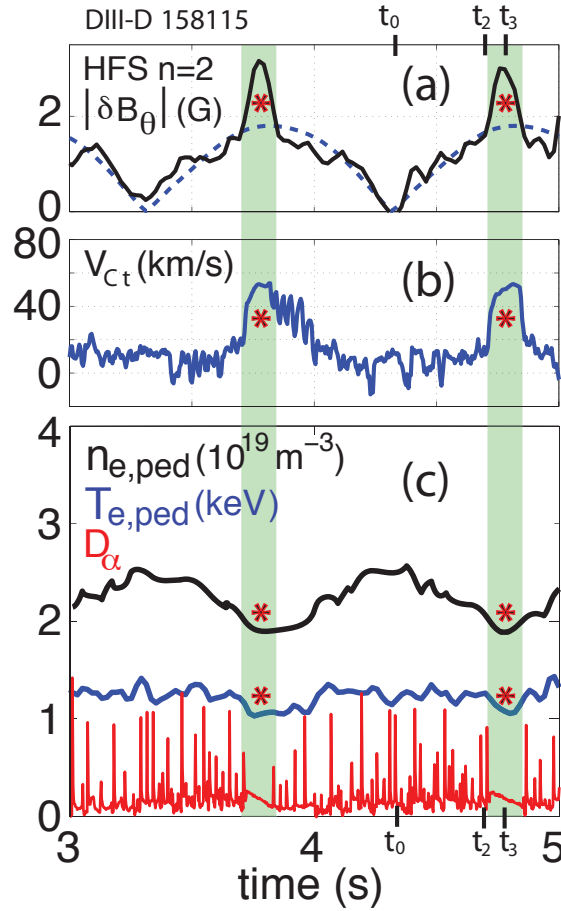


**Figure 1.** *Longest time scale.* Variations in pedestal top parameters in response to slow (1 Hz) oscillations in upper/lower I-coil phasing that modulate the amplitude of the externally imposed  $n = 2$  poloidal magnetic field components  $|\delta B_\theta|$  in DIII-D [14, 15]. The imposed RMPs vary from a minimally coupled RMP spectrum at 3.3 s to a maximally coupled spectrum at 3.7 s and again from 4.3 to 4.7 s. The  $|\delta B_\theta|$  in (a) is measured externally, just above the tokamak HFS midplane with plasma present. The solid line in (a) indicates the complete  $n = 2$   $|\delta B_\theta|$  response including the slow 1 Hz variations arising directly from modulating the I-coils. The dashed line is a trend-line fit without including the extra\* increase observed during ELM suppression. The (b) and (c) parts of the figure show plasma responses to the changing  $|\delta B_\theta|$ . Sharp peaks in the  $D_\alpha$  signal indicate ELM crashes. Green shaded vertical bands indicate times where ELM suppression occurs. Red asterisks (\*) indicate parts of figures emphasized in the text. Shorter time intervals around the 4.7 s bifurcation are shown in Figs. 5, 6.

magnetic island width, and 9) finally, the RMP-induced flutter transport effects that can reduce pedestal top gradients, stabilize P-B modes and thereby suppress ELMs. The penultimate section provides a synopsis of the main physical processes involved in the sequential stages of this new model of ELM-crash-induced ELM suppression by RMPs and the parameter conditions required for their validity. The final section summarizes the primary results obtained with this new model and the key criteria for achieving RMP suppression of type I ELMs in these near threshold  $n = 2$  experiments [14, 15].

## 2. Forced magnetic reconnection (FMR) theory

*Key Elements of FMR theory.* When three-dimensional RMPs are applied to an axisymmetric tokamak plasma it becomes metastable — two states are possible. The “high slip” state [16, 17] has large “flow screening” (shielding) of RMPs at  $q = m/n$  rational surfaces with little magnetic reconnection there — because the magnetic field that is nearly frozen into the plasmas’ rapidly moving electron fluid slips past and responds weakly to the stationary RMPs. The other, “low slip” state has little or no electron fluid flow at a rational surface and significant RMP field penetration there that can produce a large tearing-type reconnection response and a 3-D magnetic island — because when the electron fluid is nearly stationary the internal magnetic field responds strongly to the RMPs at rational surfaces. These two states and bifurcations between them are described by forced magnetic reconnection theory [16]–[24]. The original theory [18] for this “Taylor problem” was developed for a sheared magnetic field in a resistive magnetohydrodynamic (MHD) slab model that had no equilibrium plasma flows. Subsequently, cylindrical models with flows were developed for the mode-locking induced by a resonant field error [16] and the state bifurcations it can induce [17], including diamagnetic flow effects [19]–[23]. A comprehensive model that explores the temporal and spatial development of FMR that is applicable to the magnetic geometry, low collisionality and parameters in tokamak edge plasmas is being developed [24]. The main effects this tokamak FMR model introduces are: 1) dynamical effects on successively longer time scales, 2) radial transport of electrons induced by magnetic flutter, 3) low collisionality kinetic effects, 4) electron temperature gradient effects, and 4) near-separatrix magnetic geometry effects (via some order unity numerical factors).

*Magnetic field perturbations in the two states in DIII-D.* Figure 2 shows one-fluid linear numerical modeling results from M3D-C1 [25] for the radial dependence of the RMP-induced  $m/n$  radial magnetic field perturbations  $B_{mn}$  before bifurcation (at  $t_2 = 4701$  ms in Fig. 1) and well after it in the ELM suppressed state (at  $t_3 = 4781$  ms). Here and henceforth  $B_{mn}$  represents M3D-C1 modeling results while  $\delta B_\theta$  represents the experimentally measured  $n = 2$  HFS perturbed field responses. Before bifurcation the  $B_{mn}$  values are quite small at all their respective  $q = m/n$  rational surfaces in the plasma edge. This indicates high slip states with little magnetic reconnection at all these rational surfaces. After bifurcation the  $B_{mn}$  are still small at most rational surfaces. However, after bifurcation the modeled  $B_{82}$  value at the  $m/n = 8/2$  surface has increased to about 80 % of its RMP-induced vacuum value there. This indicates a low slip state with significant RMP penetration and magnetic reconnection that produces a large tearing response [14] at the 8/2 surface. The edge pressure gradient and bootstrap current cause increased gradients and magnitudes of  $B_{mn}$  at radii smaller than their respective rational surfaces in the  $0.9 < \rho_N < 0.97$  region. These are called “kink” responses. The kink-induced larger  $B_{mn}$  between rational surfaces are important in predicting the drive for the ELM-crash-induced magnetic reconnection discussed in sections 5 and 8, and the RMP-induced magnetic flutter transport discussed in section 9.

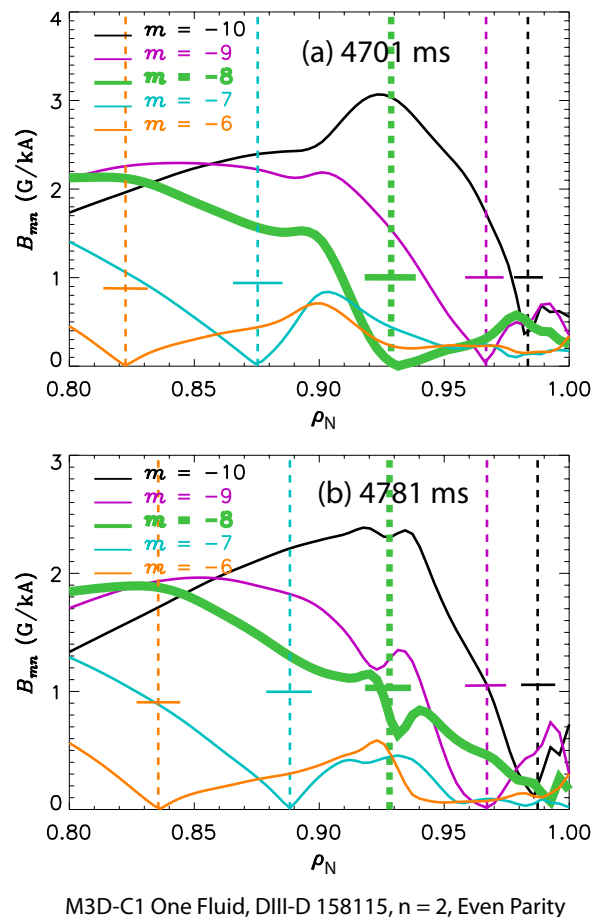


**Figure 2.** Resonant radial magnetic perturbation profiles  $B_{mn}(\rho)$  are obtained from one-fluid M3D-C1 [25] modeling in the edge of DIII-D [14, 15] at (a)  $t_2 = 4701$  ms (just before the bifurcation in Fig. 1) and (b)  $t_3 = 4781$  ms (where the maximum responses occur during ELM suppression in Fig. 1). The  $B_{mn}$  are strongly flow screened at all rational surfaces — except for the significantly penetrated 8/2 response during suppression. The normalized minor radius is  $\rho_N \equiv \rho/a$ , which is unity at the separatrix. Horizontal bars at each rational surface indicate the vacuum  $B_{mn}^{\text{vac}}$  values there.

*Magnetic field model and flux-based coordinates.* The lowest order axisymmetric magnetic field model used in the tokamak FMR model [24] is written in terms of its helical (hel) and magnetic shear (sh) components in the vicinity of a  $q(\rho_{m/n}) = m/n$  rational surface:  $\mathbf{B}_0 \equiv \mathbf{B}_{\text{hel}} + \mathbf{B}_{\text{sh}} = \nabla\alpha \times \nabla\psi_p + (q - m/n)\nabla\psi_p \times \nabla\theta$ . Here,  $\psi_p$  is the poloidal (p) magnetic flux,  $\alpha \equiv \zeta - (m/n)\theta$  is the helical angle perpendicular to  $\mathbf{B}_{\text{hel}}$  within a flux surface, and  $\theta$  and  $\zeta$  are straight-field-line poloidal and toroidal angles. The magnetic-flux-based radial coordinate used in most of this paper is the average minor radius  $\rho \equiv \sqrt{\psi_t/\pi B_{t0}}$  (in cm) which is based on the toroidal (t) magnetic flux  $\psi_t$  it encloses. The average minor radius of the separatrix is  $a \simeq 80$  cm for discharge 158115 in DIII-D [14, 15]. (The corresponding midplane minor radius is about 59 cm.) The toroidal flux is related to the poloidal flux by  $q(\rho) \equiv (d\psi_t/d\rho)/(d\psi_p/d\rho) \sim \rho B_{t0}/R_0 B_p$ . To this axisymmetric magnetic field a  $m/n$  helical Fourier component magnetic perturbation  $\delta\mathbf{B}_{m/n} \sim e^{in\alpha}$  is added to produce a total  $\mathbf{B} \equiv \mathbf{B}_0 + \delta\mathbf{B}_{m/n}$ .

The magnitude of the flux-surface-average (FSA,  $\langle \cdot \cdot \rangle$ ) of this helically-resonant radial component is  $B_{mn}(\rho) \equiv |e^{-in\alpha} \nabla \rho \cdot \delta \mathbf{B}_{m/n}|$  whose radial variations are modeled by M3D-C1 and shown in Fig. 2.

*Model for  $B_{mn}(\rho)$ .* A simple, analytic-based model for  $B_{mn}$  is used to facilitate analytic evaluations of the magnetic field structure and magnetic islands produced by RMPs. Near a rational surface  $B_{mn}(\rho)$  will be represented by (for  $x^2/L_{\delta B_{\pm}}^2 \lesssim 1$ )

$$B_{mn}(x) = B_{mn}^{\text{vac}} \sqrt{f_{\text{scr}}^2 + x^2/L_{\delta B_{\pm}}^2}, \quad x \equiv \rho - \rho_{m/n}, \quad (1)$$

$$f_{\text{scr}} \equiv B_{mn}^{\text{res}}/B_{mn}^{\text{vac}} = B_{mn}(0)/B_{mn}^{\text{vac}}, \quad \text{flow screening factor.} \quad (2)$$

Here,  $x$  is the toroidal-flux-surface-based average radial distance (in cm) from the rational surface,  $f_{\text{scr}}$  is the factor by which flow screening reduces the  $B_{mn}$  at the rational surface from its vacuum value there and  $L_{\delta B_{\pm}} \equiv |d \ln B_{mn}(\rho)/d\rho|_{\pm}^{-1}$  is the gradient scale length of  $B_{mn}$  away from the rational surface outboard (+) and inboard (-) of this surface. The RMP-induced  $B_{mn}(\rho)$  shown in Fig. 2 will be represented by  $f_{\text{scr}} \simeq 0.02$  for the high slip strongly flow-screened states (at  $t_2 = 4701$  ms) and  $f_{\text{scr}} \simeq 0.8$  for the low slip 8/2 state (at  $t_3 = 4781$  ms) which will be referred to as a RMP-penetrated state. Both states are modeled assuming  $L_{\delta B_+} \simeq 9$  cm and  $L_{\delta B_-} \simeq 4$  cm, which are chosen so the model  $B_{82}(\rho)$  in (1) approximates the RMP-driven behavior of  $B_{82}(\rho)$  in the near vicinity of the 8/2 surface in Fig. 2(a). These modeled  $B_{82}$  profiles are shown in Figs. 3(a) and 3(c). (The detailed structure of  $B_{82}$  close to the 8/2 rational surface in Fig. 2(b) is apparently caused by a combination of the RMP-driven, tearing [17] and toroidicity-induced poloidal mode coupling responses; since these details are not critical for the present analysis they will be neglected here.)

*RMP-induced magnetic field lines and islands.* For the  $B_{mn}(x)$  model in (1) the radial field line variation  $x(\Psi_{*N}, \alpha)$  induced by a RMP is governed by the equation [24]  $x^4 - [\Psi_{*N} + A_{\pm} \cos^2 n\alpha] (w_0/2)^2 x^2 + (1/4) [\Psi_{*N}^2 - \cos^2(n\alpha)] (w_0/2)^4 = 0$ ; the field lines shown in Figs. 3(b) and 3(d) are obtained from solutions of this quadratic equation for  $x^2$ . Here,  $\Psi_{*N} \equiv \Psi_* / [(m/n) \delta \psi_{m/n}(0)] \simeq \Psi_* / [R_0 B_{mn}^{\text{res}}/k_{\theta}]$  is a normalized helical magnetic flux variable (i.e.,  $\Psi_*$  satisfies  $\mathbf{B} \cdot \nabla \Psi_* = 0$ ). It is  $-1$  at the center of the island,  $+1$  at the island separatrix and  $> 1$  outside the island. In these equations the coefficient  $A_{\pm} \equiv [w_0/(4f_{\text{scr}}L_{\delta B_{\pm}})]^2$  represents the effects of the radial variation of  $B_{mn}$  within an island,  $k_{\theta} \equiv m/\rho_{m/n}$  is the RMP poloidal mode number and  $R_0$  is the major radius of the reference location for the vacuum toroidal field  $B_{t0}$ . Further, the magnetic island width when  $A_{\pm}$  effects are neglected is

$$w_0 \equiv 4 \left[ \frac{L_{\text{sh}}}{k_{\theta}} \frac{B_{mn}^{\text{res}}}{B_{t0}} \right]^{1/2}, \quad \text{reference } m/n \text{ island width.} \quad (3)$$

The total island width is in general  $w \equiv (w_+ + w_-)/2$  in which  $w_{\pm} \equiv w_0[1 + A_{\pm}]^{1/2}$ .

*Radial distances.* It is important to emphasize that the “theory-based” radial distances  $x, \rho, w$  etc. quoted throughout this paper represent average radial distances in terms of the toroidal-flux-surface-based variable  $\rho \equiv \sqrt{\psi_t/\pi B_{t0}}$  (cm). On the outboard midplane of the tokamak where the magnetic flux surfaces are compressed because of

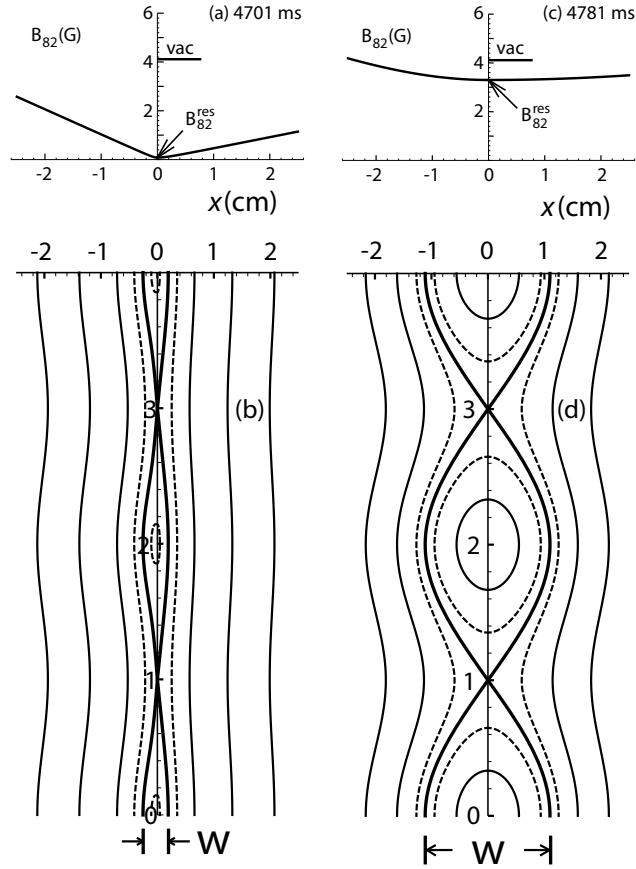


**Figure 3.** Modeled resonant magnetic perturbation profiles  $B_{82}(x)$  in the vicinity of the  $8/2$  rational surface are quite different for the (a) high slip strongly flow-screened state (at  $t_2 = 4701$  ms) and (c) low slip  $8/2$  RMP-penetrated state (at  $t_3 = 4781$  ms). Their corresponding magnetic field structures in (b) and (d) are also very different. The vertical axes in (b) and (d) are  $y \equiv n\alpha/\pi = 2\alpha/\pi$  which is a normalized angle within a flux surface that is perpendicular to  $\mathbf{B}_{\text{hel}}$ . The resistive reconnection layer width  $\delta_\eta$  on each side of the island separatrices is indicated by dashed lines in both states. The edges of the radial domains shown are just inside the distances to the adjacent  $7/2$  and  $9/2$  surfaces which occur at  $\Delta_m \simeq \pm 1/nq' \simeq \pm 2.56$  cm.

the Shafranov shift, the “laboratory” radial distances in the pedestal region are often a factor of about 2.5 smaller than these toroidal-flux-based average radial distances (see Figs. 2 and 3 in [26]). Thus, on the outboard midplane the radial domains in Fig. 3 between the adjacent rational surfaces are from about  $-1$  to  $+1$  cm and the RMP-penetrated magnetic island in Fig. 3(d) is only about 1 cm wide. Conversely, near the X-point of the divertor’s magnetic separatrix and on the inboard midplane the laboratory distances will be larger than the  $\rho$ -based values presented here.

*Island widths in DIII-D discharge 158115.* At the radius of the  $8/2$  rational surface ( $\rho_{8/2} \simeq 73$  cm)  $k_\theta \equiv m/\rho_{m/n} = 8/\rho_{8/2} \simeq 11 \text{ m}^{-1}$ , the magnetic shear length  $L_{\text{sh}} \equiv R_0q/\hat{s} \simeq 1.9$  m in which  $\hat{s} \equiv \rho q'/q|_{\rho_{8/2}} \equiv (\rho/q) (dq/d\rho)|_{\rho_{8/2}} \simeq 3.6$  and the reference toroidal magnetic field is  $B_{t0} \simeq 1.9$  T. In this DIII-D experiment the I-coil current was 4 kA and the vacuum field at the  $8/2$  surface inferred from M3D-C1 modeling was about 1.03 G/kA, as indicated by the green horizontal bars at  $\rho_N \simeq 0.93$  in Fig. 2 and at  $x = 0$

in Fig. 3. In the high slip flow-screened state in Figs. 3(a) and 3(b), the resonant field at the 8/2 rational surface is  $B_{8/2}^{\text{res}} \equiv B_{8/2}(\rho_{8/2}) = B_{8/2}(x = 0) \simeq 0.02 \times 1.03 \times 4 \simeq 0.082$  G. This yields a reference island width of  $w_0 \simeq 0.35$  cm and since  $A_+ \simeq 0.23$  and  $A_- \simeq 1.2$  the total radially asymmetric high slip (subscript hs) island width is  $w_{\text{hs}} \simeq 0.45$  cm. In the low slip (subscript ls) RMP-penetrated state in Figs. 3(c) and 3(d)  $B_{8/2}^{\text{res}} \simeq 0.8 \times 1.03 \times 4 \simeq 3.3$  G and since  $A_{\pm}^2 \ll 1$  the corresponding island widths are  $w_{\text{ls}} \simeq w_0 \simeq 2.2$  cm. These predicted half-island widths  $w/2$  are significantly less than the distances to the adjacent  $m \pm 1$  surfaces, which are estimated from the Taylor series expansion  $q(\rho_{m/n} + \Delta_m) \simeq q(m/n) + \Delta_m q' + \dots$  to be  $\Delta_m \simeq [(m \pm 1)/n - m/n]/q' \simeq \pm 1/(nq') \simeq \pm 2.56$  cm, or  $\delta\rho \sim \pm 0.04 a \simeq \pm 3.2$  cm from Fig. 2. These  $\Delta_m$  distances approximately bound the radial domains of the graphs in Fig. 3. Thus, the predicted islands on adjacent rational surfaces in DIII-D discharge 158115 [14, 15] in both the high slip and low slip states are well separated and shouldn't produce much magnetic stochasticity. As discussed in the preceding paragraph, the corresponding laboratory distances on the outboard midplane are about a factor of 2.5 smaller than the island width and  $\Delta_m, \delta\rho$  distances quoted in this paragraph.

*Periodicity lengths of field lines.* Figures 3(b) and 3(d) show that as one moves along magnetic field lines outside magnetic islands (i.e., for  $|x| > w/2$ ) their radial distance off the rational surface varies approximately sinusoidally with increasing  $\alpha \equiv \pi y/2$ . This radial motion is called ‘‘magnetic flutter.’’ The FSA periodicity length along magnetic field lines over which radial variations occur is in general [24]  $L_{\parallel} \equiv \oint d\alpha \langle dl/d\alpha \rangle = \oint d\alpha \langle B/\mathbf{B}_0 \cdot \nabla \alpha \rangle \simeq (L_{\text{sh}}/k_{\theta}) \oint n d\alpha/x(\Psi_{*N}, \alpha)$ . Neglecting  $A_{\pm}$  asymmetry effects, the radial flutter of a field line is in general governed by  $x(\Psi_{*N}, \alpha) = \pm(w_0/2) [(\Psi_{*N} + \cos n\alpha)/2]^{1/2} = x_0 [(\Psi_{*N} + \cos n\alpha)/(\Psi_{*N} + 1)]^{1/2}$ . Here,  $x_0 \equiv x(\Psi_{*N}, 0) = \pm(w_0/2) [(1 + \Psi_{*N})/2]^{1/2}$  is the radial distance of the field line from the rational surface at  $\alpha = y = 0$ . Far outside a magnetic island where  $\Psi_{*N} \gg 1$ , the field line equation is  $x \simeq x_0 [1 + (\cos n\alpha - 1)/(2\Psi_{*N}) + \dots]$  and the periodicity length is  $L_{\parallel} \simeq 2\pi L_{\text{sh}}/(k_{\theta} x_0)$ . At the  $x_0 \rightarrow \Delta_m/2 \simeq 1.28$  cm midpoint between the 7/2 and 8/2 or 8/2 and 9/2 rational surfaces in 3(b) and 3(d), this periodicity length is  $L_{\parallel} \simeq 90$  m. Within a magnetic island (i.e., for  $|x_0| < w/2$ ) the length over which magnetic field lines close on themselves is [24]  $L_w \equiv \oint d\alpha \langle B/\mathbf{B}_0 \cdot \nabla \alpha \rangle = (L_{\text{sh}}/k_{\theta}) \oint n d\alpha/x(\Psi_{*N}, \alpha) \simeq [8\pi L_{\text{sh}}/(k_{\theta} w_0)] [(2/\pi)K(k)]$ . Here,  $K(k) \geq \pi/2$  is the complete elliptic integral of the first kind with argument  $k \equiv |x_0|/(w_0/2) < 1$ . The lengths of these periodic, radially fluttering closed field lines within the islands in the high slip and low slip cases in DIII-D discharge 158115 [14, 15] are  $L_w \gtrsim 700$  m in 3(b) and  $L_w \gtrsim 200$  m in 3(d).

*Radial magnetic flutter and its effects.* When combined with finite electron collisionality the radial magnetic flutter of magnetic field lines both outside and inside magnetic islands produces non-ambipolar FSA radial transport of electrons [28, 29]. Flutter transport is important because the effective electron collision length  $\lambda_{e \text{ eff}} \simeq 90$  m (see section 3) is of the order of or shorter than the long periodicity lengths  $L_{\parallel}$  and  $L_w$ . This collisional electron regime together with radial flutter transport [28, 29] cause  $T_e$  to not be constant along the field lines in 3(b) and 3(d) (see section 9).

*Reconnection layer width.* Magnetic field lines only reconnect in a very thin singular layer [16]–[24] around a rational surface where magnetic field diffusion induced by the plasma resistivity invalidates the ideal MHD frozen flux theorem. The radial half-width of the 8/2 resistive layer can be approximated by [16, 17, 24]  $\delta_\eta \simeq \rho_{8/2}/S^{1/3} \simeq 0.14$  cm where  $S \equiv \tau_R/\tau_A \simeq 1.3 \times 10^8$  is the Lundquist number, and  $\tau_R \equiv \rho_{8/2}^2/D_\eta \simeq 3.8$  s and  $\tau_A \equiv L_{\text{sh}}/mc_A \simeq 2.9 \times 10^{-8}$  s are global resistive and shear-Alfvén times. The effective magnetic field diffusivity induced by the neoclassical parallel resistivity is [24]  $D_\eta \equiv \bar{g}^{\rho\rho}\eta_{\parallel}^{\text{nc}}/\mu_0 \simeq 0.14$  m<sup>2</sup>·s<sup>-1</sup>. Here,  $\bar{g}^{\rho\rho} \simeq 2.1$  is a geometric factor that represents the poloidal average of the radial compression (on the outboard side of the tokamak) and expansion (on the inboard side) of magnetic flux surfaces, and the parallel neoclassical resistivity can be obtained from  $\eta_{\parallel}^{\text{nc}}/\mu_0 \simeq 0.066$  m<sup>2</sup>·s<sup>-1</sup>. The following parameters at the 8/2 rational surface [15] have been used in evaluating these quantities:  $n_e = 2.2 \times 10^{19}$  m<sup>-3</sup>,  $n_i = 1.3 \times 10^{19}$  m<sup>-3</sup>,  $Z_{\text{eff}} = 2.6$ ,  $T_e = 1150$  eV and  $T_i = 1600$  eV (see Fig. 4 below).

*Reconnection states.* The resistivity-induced reconnection region is localized about the magnetic island separatrix, as indicated by dashed lines in Figs. 3(b) and 3(d). While the widest reconnection region occurs around the island X-point, reconnection occurs all along the island separatrix which is the three-dimensional  $q = 8/2$  surface here. Outside these thin dashed lines the ideal MHD frozen flux theorem is still roughly applicable because reconnection of magnetic field lines is small there. In the high slip strongly flow-screened state in Fig. 3(b) the magnetic island width  $w_{\text{hs}} \simeq 0.45$  cm is slightly larger than the total width  $2\delta_\eta \simeq 0.3$  cm of the reconnection layer. In the low slip RMP penetrated state in Fig. 3(d) the island width  $w_{\text{ls}} \simeq 2.2$  cm is much larger than the total resistive layer width  $2\delta_\eta \simeq 0.3$  cm. The low slip state is in what is called the (nonlinear) Rutherford regime [30] because  $w_{\text{ls}} \gg 2\delta_\eta$ . The temporal evolution of the island width  $w$  in this regime is discussed in section 8. Rigorously speaking, the linear M3D-C1 results in Fig. 2 are only applicable for island widths smaller than the resistive layer widths. However, since the theoretically inferred magnetic islands on adjacent  $m/2$  rational surfaces do not overlap, the tearing responses and consequent magnetic islands on the rational surfaces can all be treated approximately independently. In this situation the M3D-C1 results can apparently be extended, at least roughly, into the nonlinear Rutherford regime — as is done in this paper.

*General properties of the two states in DIII-D.* Figure 3 illustrates that: 1) in the high slip state at  $t_2 = 4701$  ms where flow screening is large the radial component of the resonant magnetic field  $B_{82}^{\text{res}} \simeq 0.082$  G is very small on the 8/2 rational surface and while there is a magnetic island there, it is quite thin and barely wider than the total resistive layer width  $2\delta_\eta$ ; 2) in the low slip state at  $t_3 = 4781$  ms where flow screening is minimal the 8/2 RMP is nearly fully penetrated, and the large magnetic perturbation at the rational surface  $B_{82}^{\text{res}} \simeq 3.3$  G produces a (nonlinear) moderate width magnetic island which is much wider than the total resistive layer width  $2\delta_\eta$ , and 3) both inside and particularly outside these magnetic islands there is always significant radial “magnetic flutter” of the magnetic field lines induced by the RMPs.

### 3. Flow screening

*Modeling flow screening.* The preceding section discussed the magnetic topology of the distinct high slip strongly flow-screened and low slip RMP-penetrated states inferred from analysis and modeling of data from DIII-D discharge 158115 [14, 15]. This section describes the linear model that is usually used to describe the degree of flow screening of RMPs that occurs at rational surfaces for these two states and its limitations. Also, the (nonlinear) magnetic flutter transport effects that remove the electron diamagnetic flow contributions to the perpendicular electron flow frequency that justify using one-fluid M3D-C1 modeling for obtaining the  $B_{mn}$  profiles in Fig. 2 are discussed.

*Linear flow screening model.* In linear models of FMR the predicted factor by which the radial component of the externally applied RMP field  $B_{mn}$  is reduced from its vacuum value  $B_{mn}^{\text{vac}}$  at the  $\rho_{m/n}$  rational surface can be written as [17, 24]

$$f_{\text{scr}} \equiv \frac{B_{mn}^{\text{res}}}{B_{mn}^{\text{vac}}} = \left| \frac{\rho_{m/n} \Delta'_{\text{RMP } m/n}}{-\rho_{m/n} \Delta'_{m/n} - i n \Omega_e^\alpha \tau_\delta} \right|. \quad (4)$$

Here,  $\Delta'_{m/n} \equiv d \ln B_{mn}^{\text{tear}} / d\rho|_+ - d \ln B_{mn}^{\text{tear}} / d\rho|_- \simeq -2 k_\theta = -2 m / \rho_{m/n}$  is the usual tearing mode stability parameter [31, 32], which is usually stabilizing ( $< 0$ ) in the pedestal region. The analogous and very important RMP-drive parameter is

$$\Delta'_{\text{RMP } m/n} \equiv \frac{m \mu_0 J_{mn}}{i \bar{g}^{\rho\rho} B_{mn}^{\text{vac}}} \simeq \frac{1}{L_{\delta B_+}} + \frac{1}{L_{\delta B_-}}, \quad (5)$$

$$J_{mn} \equiv \frac{\bar{g}^{\rho\rho}}{-i m \mu_0} \int_-^+ d\rho \frac{d^2 B_{mn}}{d\rho^2}. \quad (6)$$

The parameter in (5) represents the resonant parallel current density  $J_{mn}$  caused by the discontinuity in the radial derivatives of the radial perturbation  $B_{mn}$  across the rational surface induced by the  $m/n$  RMP in the ideal MHD limit. The singular layer relaxation time in (4) is [17, 24]  $\tau_\delta \simeq 2 \delta_\eta \rho_{m/n} / D_\eta = 2 S^{2/3} \tau_A$ . Rigorously speaking, the ideal MHD limit is  $\tau_\delta \rightarrow \infty$ . As long as  $\Omega_e^\alpha \neq 0$ , in the ideal MHD limit  $f_{\text{scr}} = 0$ . The low slip state in Fig. 3(a) is close to the ideal MHD limit because  $f_{\text{scr}} \ll 1$  there. Thus, (5) and (6) can be used to approximately determine  $\Delta'_{\text{RMP } m/n}$  in the low slip state. The usually small corrections due to cylindrical-geometry-type effects ( $\sim 1/m$ ) and a spatially varying magnetic shear [33] are neglected here.

*Flow screening frequency.* The relevant rotation frequency  $\Omega_e^\alpha$  of the electron fluid flow velocity  $\mathbf{V}_e$  in (4) is in the  $\nabla\alpha \equiv \nabla\phi - (m/n)\nabla\theta$  direction, which is perpendicular to the helically resonant field  $\mathbf{B}_{\text{hel}}$  on a magnetic flux surface. Most generally it is [24]

$$\begin{aligned} \Omega_e^\alpha(\rho) &\equiv \nabla\alpha \cdot \mathbf{V}_e = - \left[ \frac{d\Phi_0}{d\psi_p} - \frac{1}{n_e e} \frac{dp_e}{d\psi_p} - \frac{0.71}{e} \frac{dT_e}{d\psi_p} \right] \\ &\simeq \omega_{\perp e} \equiv \omega_E + \omega_{*e}, \quad \omega_E \equiv \frac{E_\rho}{R B_p}, \quad \omega_{*e} \equiv \frac{1}{n_e e R B_p} \frac{dp_e}{d\rho}. \end{aligned} \quad (7)$$

Here,  $E_\rho(\rho) \equiv -d\Phi_0/d\rho$  is the equilibrium radial electric field,  $p_e(\rho) = n_e T_e$  the electron pressure,  $T_e(\rho)$  the electron temperature,  $\omega_{\perp e}$  the perpendicular  $\mathbf{E} \times \mathbf{B}$  plus electron diamagnetic flow frequency,  $\psi_p(\rho)$  the poloidal flux function and  $\psi'_p \equiv d\psi_p(\rho)/d\rho =$

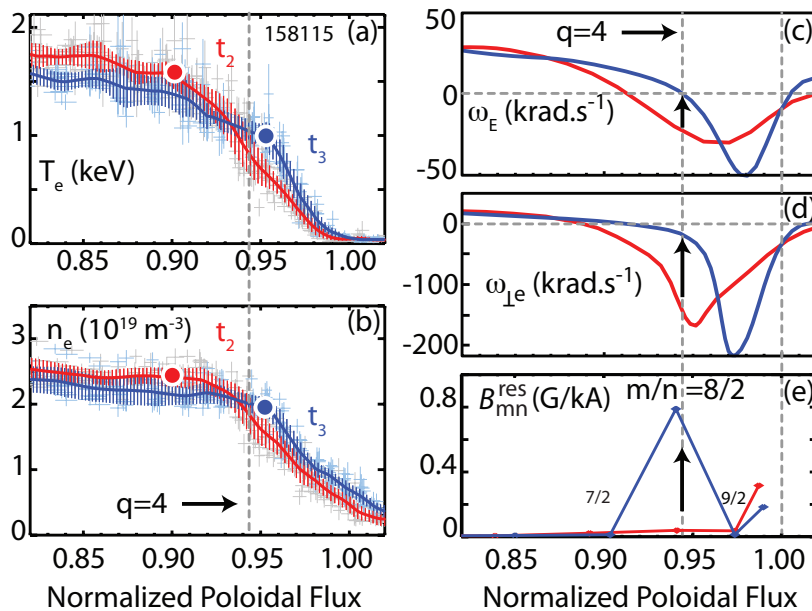


**Figure 4.** Radial profiles of key parameters change significantly from before ELM suppression (red,  $t_2 = 4701$  ms) to the saturated state during it (blue,  $t_3 = 4781$  ms): (a) electron temperature  $T_e$ ; (b) electron density  $n_e$ ; (c)  $\mathbf{E} \times \mathbf{B}$  frequency  $\omega_E$ ; (d) electron fluid perpendicular flow frequency  $\omega_{\perp e}$  for  $n_e$  and  $T_e$  profiles in (a) and (b); and (e) resonant field amplitudes  $B_{mn}^{\text{res}}$  at rational surfaces calculated by the one-fluid M3D-C1 [25] model. The radial coordinate here is the normalized poloidal magnetic flux  $\psi_p(\rho)/\psi_p(a)$ , which is about 0.01 greater than the normalized coordinate  $\rho_N \equiv \rho/a \simeq 0.93$  at the 8/2 rational surface in Fig. 2. Circles in (a) and (b) denote the radial location at the “pedestal top.” This figure is an adapted and modified version of Fig. 3 in Ref. [15], primarily by its inclusion of more recent and precise M3D-C1 modeling results in (e).

$B_p(\rho, \theta) R(\rho, \theta)$  has been used. The electron flow frequency  $\Omega_e^\alpha$  in (7) is more complete than the typically used  $\omega_{\perp e}$  [22, 23, 25] due to its inclusion [24] of the usually neglected electron thermal force effects [34] induced by the electron temperature gradient.

*Linear regime model approximations.* The linear model flow-screening formula in (4) is only rigorously valid if the magnetic island width is less than the full width of the reconnection layer, i.e.,  $w \ll 2\delta_\eta$ . This criterion is not satisfied for either of the DIII-D states discussed in the preceding section. However, the formula in (4) is often used to estimate flow-screening effects; doing so implicitly assumes it is approximately valid in the reconnecting layer  $\delta_\eta$  around a (nonlinear) magnetic island’s separatrix, as illustrated in Fig. 3. This is apparently a reasonable approximation with the caveat that usually flutter transport effects cause  $\Omega_e^\alpha \rightarrow \omega_E$  in the  $\delta_\eta$  layer, as discussed below.

*Flow frequency profiles in the two DIII-D states.* The electron temperature and density profiles in the pedestal region before and during ELM suppression in DIII-D discharge 158115 [14, 15] are shown in Figs. 4(a) and 4(b). The  $\omega_E$  and  $\omega_{\perp e}$  profiles that result from these profiles plus the  $E_\rho$  profile obtained from CER measurements [35, 36] of the carbon flows and pressure gradient are shown in Figs. 4(c) and 4(d). These figures indicate that both  $|\omega_E|$  and  $|\omega_{\perp e}|$  decrease dramatically at the 8/2 rational

surface in the ELM suppressed state at  $t_3 = 4781$  ms. Figure 4(e) shows the 8/2 RMP has penetrated significantly in this  $|\omega_E| \simeq 0$  low slip state at the 8/2 rational surface.

*Magnetic flutter electron transport diffusivity.* The suggestion that magnetic flutter produces a radial electron thermal diffusivity  $\chi_{er} \simeq \chi_{e\perp} + (\tilde{B}_r/B)^2 \chi_{e\parallel}$  was introduced phenomenologically in Ref. [27]. The more general, kinetically-derived fundamental diffusivity induced by magnetic flutter at a  $m/n$  rational surface can be written as [28]  $D_{et}(\rho_{m/n}) \simeq 0.85 (v_{Te}^2/\nu_{e\text{eff}}) (B_{mn}^{\text{res}}/B_{t0})^2$ . Here,  $v_{Te} \equiv \sqrt{2T_e/m_e}$  is the electron thermal speed and the effective electron collision rate is  $\nu_{e\text{eff}} \equiv \nu_e/(f_c B_{\text{max}}/B_{t0})$  in which  $\nu_e \simeq 5 \times 10^{-11} (n_e Z_{\text{eff}}/[T_e(\text{eV})]^{3/2}) (\ln \Lambda/17) \text{ s}^{-1}$  is the 90° electron scattering collision rate. The  $f_c B_{\text{max}}/B_{t0} < 1$  term represents the flow-weighted small fraction of circulating electrons that carry the parallel current in the tokamak edge region; the rate of scattering of electrons out of this small region of velocity space increases the effective electron collision rate by the inverse of this factor. At the 8/2 rational surface in DIII-D discharge 158115 [14, 15]  $v_{Te} \simeq 2 \times 10^7 \text{ m} \cdot \text{s}^{-1}$ ,  $\nu_e \simeq 7.4 \times 10^4 \text{ s}^{-1}$ ,  $f_c B_{\text{max}}/B_{t0} \simeq 1/3$  and hence  $\nu_{e\text{eff}} \simeq 3\nu_e \simeq 2.2 \times 10^5 \text{ s}^{-1}$ . These parameters produce a 90° electron collision length  $\lambda_e \equiv v_{Te}/\nu_e \simeq 270 \text{ m}$  and an effective electron collision length for flutter transport of  $\lambda_{e\text{eff}} \equiv v_{Te}/\nu_{e\text{eff}} \simeq 90 \text{ m}$ . The fundamental flutter diffusivity for radial electron transport near the 8/2 surface in DIII-D discharge 158115 can be written as [24, 28]

$$D_{et}(\rho_{8/2}) \simeq 1.5 \times 10^9 \left( \frac{B_{82}^{\text{res}}}{B_{t0}} \right)^2 \text{ m}^2 \cdot \text{s}^{-1}. \quad (8)$$

This electron diffusivity only applies within the layer width [28]  $\delta_{\parallel t} \simeq 3.2 L_{\text{sh}}/(k_\theta \lambda_e)$  around a rational surface. Since  $\delta_{\parallel t} \simeq 0.2 \text{ cm}$  in DIII-D discharge 158115 [14, 15], it is slightly larger than the reconnection layer width  $\delta_\eta \simeq 0.14 \text{ cm}$  at the 8/2 surface.

*Flutter transport effects on perpendicular electron flow at rational surfaces.* As discussed in section 2, in the ELMing equilibrium at  $t_2 = 4701$  ms the magnitude of the flow-screened resonant  $B_{82}^{\text{res}}$  is estimated to be about 0.082 G, which using (8) yields  $D_{et}(\rho_{8/2}) \simeq 0.03 \text{ m}^2 \cdot \text{s}^{-1}$ . Even though this diffusivity is small, since  $\delta_{\parallel t} \gtrsim \delta_\eta$  it relaxes the electron density, temperature and hence pressure gradients in the thin layer  $\delta_\eta$  on the very short time scale  $\tau_{\text{flutt}} \sim \delta_\eta^2/D_{et} \simeq 0.07 \text{ ms}$ . Since ion gyroradii and banana widths are much larger than  $\delta_{\parallel t}$  and  $\delta_\eta$ , the ion response in the resistive layer is negligible. Thus, the nonlinear flutter transport causes the  $p_e$  and  $T_e$  gradient terms in (7) to become negligible in the reconnection layer both before and during ELM suppression, i.e.,

$$\Omega_e^\alpha \simeq \omega_{\perp e} \rightarrow \omega_E, \text{ in } \delta_{\parallel t} \gtrsim \delta_\eta \text{ layers at rational surfaces.} \quad (9)$$

This effect only applies in thin electron pressure flattening layers  $\delta_{\parallel t} \gtrsim \delta_\eta$  around rational surfaces, i.e., in slightly wider regions than those between the dashed lines around the magnetic separatrices in Figs. 3(b) and 3(d). Physically, this means that at the resonant surface the electron fluid rotates in the perpendicular ( $\nabla\alpha$ ) direction with the  $\mathbf{E} \times \mathbf{B}$  frequency  $\omega_E$ , i.e., without electron diamagnetic flow effects. Since on the DIII-D outboard midplane these electron pressure gradient flattening regions are only about  $2\delta_{\parallel t}/2.5 \sim 0.16 \text{ cm}$  wide, they are unlikely to be resolvable with present diagnostics or M3D-C1 modeling. This flutter transport effect is fully dissipative

and applicable [28, 24] as long as the effective electron collision rate  $\nu_{e\text{eff}}$  is of order or exceeds the frequency of the electron fluid relative to the stationary RMPs, i.e.,  $\nu_{e\text{eff}} \gtrsim \omega \equiv n\Omega_e^\alpha \simeq 2\omega_{\perp e}$ . This condition is well satisfied at most of the edge rational surfaces in Fig. 4(d). However, it is only marginally appropriate at the 8/2 surface where  $\nu_{e\text{eff}}/(2\omega_{\perp e}) \simeq (2 \times 10^5)/(2 \times 1.3 \times 10^5) \simeq 0.85$ , or about  $\nu_{e\text{eff}}/(2\Omega_e^\alpha) \simeq 0.55$  including the  $0.71 dT_e/d\rho$  effect. When this criterion is not satisfied,  $D_{\text{et}}(\rho_{m/n})$  becomes a factor of  $[\nu_{e\text{eff}}/(n\Omega_e^\alpha)]^2$  smaller [24]. Since nonlinear magnetic flutter transport effects remove the electron diamagnetic flow contributions to the perpendicular electron flow frequency near the rational surfaces (i.e., between the dashed lines in Fig. 3), they justify using one-fluid instead of two-fluid linear M3D-C1 modeling for obtaining the  $B_{mn}$  profiles in Fig. 2, except possibly at the 8/2 surface in Fig. 2(a) where  $f_{\text{scr}}$  could be a bit smaller.

*Parameters at 8/2 rational surface.* At the radius  $\rho_{8/2} \simeq 73$  cm of the 8/2 rational surface, assuming the radial gradient of the current is small there [32],  $\rho_{8/2}\Delta'_{8/2} \simeq -16$ . For the  $L_{\delta B_+} = 9$  cm and  $L_{\delta B_-} = 4$  cm values used in obtaining the magnetic field structures in Fig. 3, the definition in (5) yields  $\rho_{8/2}\Delta'_{\text{RMP } 8/2} \simeq 26.4$ . The strong  $B_{mn}$  kink responses in the radial region  $0.9 < \rho_N < 0.97$  are apparently what cause  $\Delta'_{\text{RMP } 8/2}$  to exceed  $|\Delta'_{8/2}|$  there. Using the definitions and parameter values at the 8/2 resonant surface given in the previous section, the predicted layer relaxation time is  $\tau_\delta \simeq 0.014$  s.

*Flow screening regimes.* Before bifurcation the  $\mathbf{E} \times \mathbf{B}$  electron flow frequencies at the 7/2, 8/2, 9/2 surfaces in Fig. 4(c) are  $\omega_E \sim (15, -25, -15)$  krad  $\cdot$  s $^{-1}$ . Since using (9)  $|n\Omega_e^\alpha \tau_\delta| \rightarrow |n\omega_E \tau_\delta| \sim 420\text{--}700 \gg |\rho_{m/n}\Delta'_{m/n}| \sim 14\text{--}18$  there, the strong flow screening predicted by (4) becomes simply  $f_{\text{scr}} \simeq \rho_{m/n}\Delta'_{\text{RMP } m/n}/|n\omega_E \tau_\delta| \sim 0.04$ . This analytic-based high slip strong flow screening prediction is a factor of two larger than the  $f_{\text{scr}} = 0.02$  value for the magnetic field model used in developing Fig. 3; however, it is reasonably consistent with the  $f_{\text{scr}}$  magnitudes at the 7/2, 8/2 and 9/2 rational surfaces in Figs. 2(a) and 4(e), as well as the flow-screening at the 7/2 and 9/2 surfaces in Figs. 2(b) and 4(e). In the low slip state at  $t_3 = 4781$  ms, Fig. 4(c) shows  $\omega_E$  is close to zero at the 8/2 surface, which could be responsible for the significantly reconnected (amplified [37])  $B_{82}^{\text{res}}$  response there. Then, the analytic model prediction is  $f_{\text{scr}} \leq \Delta'_{\text{RMP } 8/2}/|\Delta'_{8/2}| \simeq 1.6$  (or smaller if  $|\Omega_e^\alpha| \rightarrow |\omega_E| \sim |\rho_{8/2}\Delta'_{8/2}|/(n\tau_\delta) \gtrsim 0.6$  krad  $\cdot$  s $^{-1}$ ). This prediction is at most a factor of two larger than the  $f_{\text{scr}} \simeq 0.8$  flow-screening factor at the 8/2 surface in Fig. 2(b). Thus, with appropriate interpretations [especially that in (9)] the often used analytic, linear flow screening factor formula in (4) can apparently be used to estimate (within a factor  $\lesssim 2$ ) the amount of flow screening in both the high slip flow-screened and 8/2 low slip RMP-penetrated states.

#### 4. RMP-induced responses to an ELM crash

*Dynamics on shorter time scales.* Up to this point the discussion has focused on characterizing the two distinct RMP-induced states of FMR: high slip with minimal reconnection before suppression and low slip with significant RMP penetration a long time (75 ms) after bifurcation. The next, critically important step is to explore the

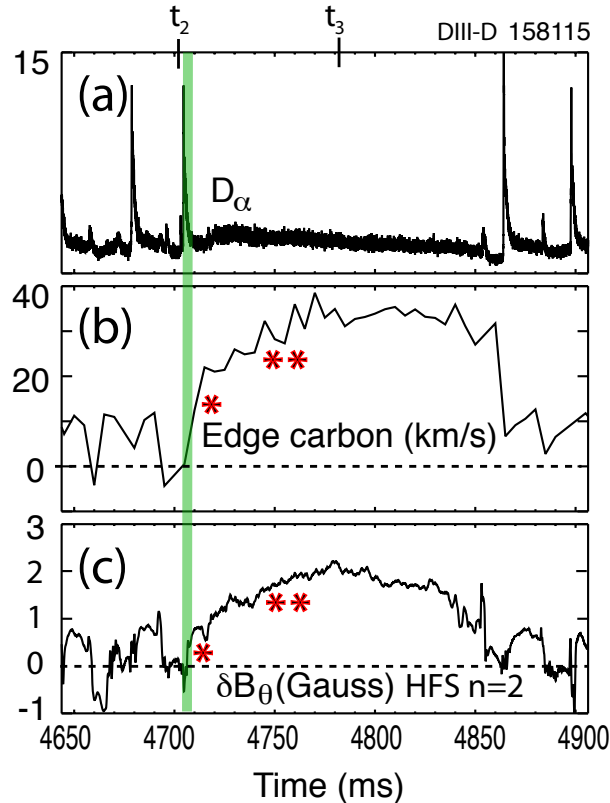


**Figure 5.** *Medium time scale:* As the maximum RMP amplitude is reached (just after  $t_2$  in Fig. 1), an ELM crash marked by the vertical green bar at 4705 ms apparently induces the bifurcation into an ELM-suppressed state during which: (a) the  $D_\alpha$  signal abruptly peaks and decays back to the noise level; (b) the edge carbon toroidal flow speed  $V_{Ct}$  inferred from C-VI emission CER measurements [35, 36] first increases fairly quickly\*, then increases more slowly\*\* up to a saturation level at about  $t_3 = 4781$  ms and finally bifurcates back to an ELMing state after 4860 ms [15]; and (c) the HFS-measured real part of  $\delta B_\theta$  apparently increases at about 4705 ms more rapidly (\*) than  $V_{Ct}$  does (\*) and then likewise increases more slowly\*\*, saturates and ultimately bifurcates [15] back to the ELMing state as the applied RMP begins decreasing.

nonlinear dynamics of the evolution from the high slip flow-screened state into the low slip RMP-penetrated state. Figures 5 and 6 show the dynamics of the carbon toroidal flow  $V_{Ct}$  in the top half of the pedestal (at  $\rho_N \sim 0.96$ , normalized  $\psi_p \sim 0.97$  [15]) and the  $n = 2$  HFS-measured magnetic response  $\delta B_\theta$ , around and shortly after the last ELM crash before bifurcation into the ELM-suppressed state. It is important to note that in Figs. 5–7 the baselines for the  $\delta B_\theta$  signals have been set to zero at 4700 ms ( $\delta t = -5$  ms in Figs 6, 7). Thus, the  $\delta B_\theta$  signals in these figures mostly represent the extra\* mainly tearing-type responses [14] in excess of the applied RMP amplitude that is evolving very slowly — see Fig. 1(a). The continuity of the tearing-type responses to the ELM crash across the different temporal averaging used in the sequentially shorter time intervals of Figs. 1, 5–7 provides confidence that this  $\delta B_\theta$  baseline setting procedure is a reasonable approach for studying dynamical processes involved in ELM suppression. In particular, it confirms that  $\delta B_\theta$  increases (not decreases) in response to the ELM crash.

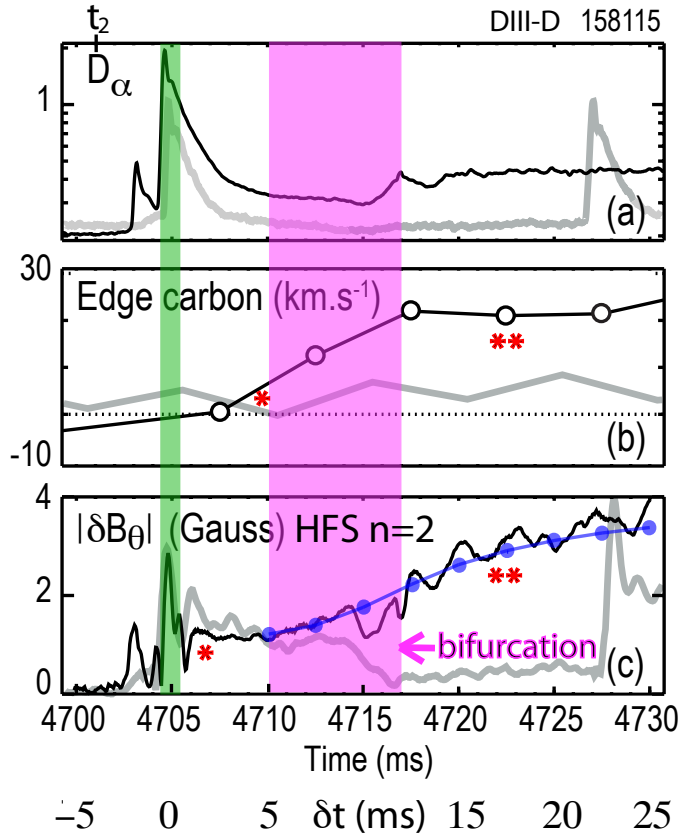


**Figure 6.** *Shortest time scale.* When the applied RMP is largest (solid lines), during the  $\delta t \simeq 5\text{--}12$  ms time interval (purple vertical bar) after the ELM crash at  $\delta t \simeq 0$  (4704.5–4705.5 ms, green vertical bar) the carbon toroidal flow  $V_{Ct}$  and extra\* HFS magnetic perturbation bifurcate into an ELM suppressed state in which  $|\delta B_\theta|$  and  $V_{Ct}$  grow slowly\*\*. The light blue dots and line in (c) show the MRE theoretical prediction (see section 8). The gray lines are analogous traces for the smallest RMP amplitude in Fig. 1, which occurs at about  $t_0 = 4300$  ms, but here time shifted by +398 ms. The gray lines show that for the smallest applied RMP the ELM that occurs at 4307 ms does not produce ELM suppression; during bifurcation (purple vertical bar)  $|\delta B_\theta|$  decays and  $V_{Ct}$  does not grow (gray lines) — up to another ELM which occurs at  $\delta t \simeq 22$  ms.

*Medium time scale response to ELM.* Figure 5 shows: 1) the extra\*  $n = 2$  HFS tearing-type  $\delta B_\theta$  and edge toroidal carbon flow  $V_{Ct}$  responses seen in Fig. 1(a) increase abruptly\*, roughly coincident with the ELM crash that occurs at about 4705 ms; 2) after the rapid increases in  $\delta B_\theta$  and  $V_{Ct}$ , these signals increase slowly\*\* up to saturation levels at about  $t_3 = 4781$  ms, then decay slowly and ultimately bifurcate [15] back to an ELMing state after 4860 ms; and 3) the abrupt  $\delta B_\theta$  increase at about 4705 ms apparently precedes the increase in  $V_{Ct}$ , whose CER measurements [36] have been averaged over 5 ms intervals. The last point is confirmed by the shorter time interval behavior shown in Figs. 6(b) and 6(c).

*Shortest time scale response to ELM.* The shortest time scale Fig. 6 shows the ELM crash preceding ELM suppression in DIII-D discharge 158115 [15] begins at about 4704.5 ms. The evolution toward bifurcation into the ELM-suppressed state following

the ELM has many stages: 1) the spike in the  $D_\alpha$  signal is coincident with an ideal MHD-type instability that causes the ELM, which will be assumed to be a peeling-ballooning (P-B) mode; 2) the accompanying  $|\delta B_\theta|$  signal reaches a peak and then decays, in about 1 ms; 3) this occurs whether or not RMPs are present (this detail is not shown here); 4) however, when RMPs are present in DIII-D discharge 158115 [15], in the subsequent  $\delta t \simeq 1\text{--}5$  ms (4706–4710 ms) time interval a transient stage occurs during which there is a sustained  $n = 2$  tearing-type  $|\delta B_\theta|$  of about 1.2 Gauss\* and the carbon flow speed  $V_{Ct}$  begins to evolve\*; 5) then during the  $\delta t \simeq 5\text{--}12$  ms (4710–4717 ms) time interval the  $|\delta B_\theta|$  and  $V_{Ct}$  responses begin to bifurcate (purple vertical bar in Fig. 6) since when the externally applied RMP is largest (just after  $t_2 = 4701$  ms in Fig. 1) they grow slowly while for the smallest applied RMP (at about  $t_0 = 4300$  ms in Fig. 1)  $|\delta B_\theta|$  decays; and 6) thereafter for the largest RMP they increase slowly\*\* while for the smallest RMP they have decayed to small, nearly constant values and another ELM occurs after about 22 ms. Thus, the key questions for achieving bifurcation into the ELM-suppressed state are: 1) how does the  $\sim 1$  ms ELM crash in the 4704.5–4705.5 ms time interval around  $\delta t = 0$  produce the tearing-type  $\delta B_\theta$  observed in the  $\delta t \simeq 1\text{--}5$  ms (4706–4710 ms) time interval?; and 2) what are the key physical processes in the  $\delta t \simeq 5\text{--}12$  ms (4710–4717 ms) time interval after an ELM crash that causes the bifurcation?

## 5. Magnetic field penetration during ELM crash

*Toroidal rotation of  $\delta B_\theta$ .* Figure 7 shows that: 1) during the 4704.5–4705.5 ms time interval (green vertical bar around  $\delta t = 0$ ) the toroidal phase angle of the extra\*  $n = 2$  magnetic perturbation  $|\delta B_\theta|$  increases almost linearly with time, which implies an initial toroidal rotation frequency of  $|\delta B_\theta|$  at the  $n = 2$  resonant surfaces of  $\omega_t^{\text{ELM}} \equiv \Delta \text{Toroidal Angle} / \Delta t \sim 2 \times 10^3 \text{ rad} \cdot \text{s}^{-1}$ ; 2) at about 4706 ms ( $\delta t \simeq 1$  ms) the toroidal phase quickly transitions into  $n = 2$  wall-locked tearing-type responses (i.e.,  $\omega_t^{\text{res}} \rightarrow 0$ ); 3) during the  $\delta t \simeq 1\text{--}5$  ms (4706–4710 ms) time interval the HFS  $n = 2$  perturbation remains locked to the laboratory (RMP) frame and the externally measured extra\*  $|\delta B_\theta|$  remains about 1.2 G larger than its value before the ELM crash (see Figs. 5–7); and 4) after the  $\delta t \simeq 5\text{--}12$  ms (4710–4717 ms) bifurcation time interval Fig. 7 shows the resonant perturbation remains firmly mode-locked to the stationary RMP frame (i.e., keeps  $\omega_t^{\text{res}} \simeq 0$ ) as  $|\delta B_\theta|$  slowly grows\*\* for the largest RMP.

*Theory of ELM-crash-induced tearing response.* At present there is no nonlinear theory or simulation for how an ideal MHD P-B mode produces a tearing-type  $n = 2$  perturbation. However, theory developed for how sawtooth and ELM crashes can seed neoclassical tearing mode (NTM) islands [38]–[40] will be applied here to describe how an ELM crash produces a tearing-type response. After adapting that nonlinear theory to the present notation, the radial component of a P-B mode ideal MHD perturbation  $B_{mn}^{\text{ELM}}$  during the ELM crash is predicted [38, 24] to induce magnetic reconnection on the resonant surface (here, the magnetic island separatrix) and thus a resonant field of

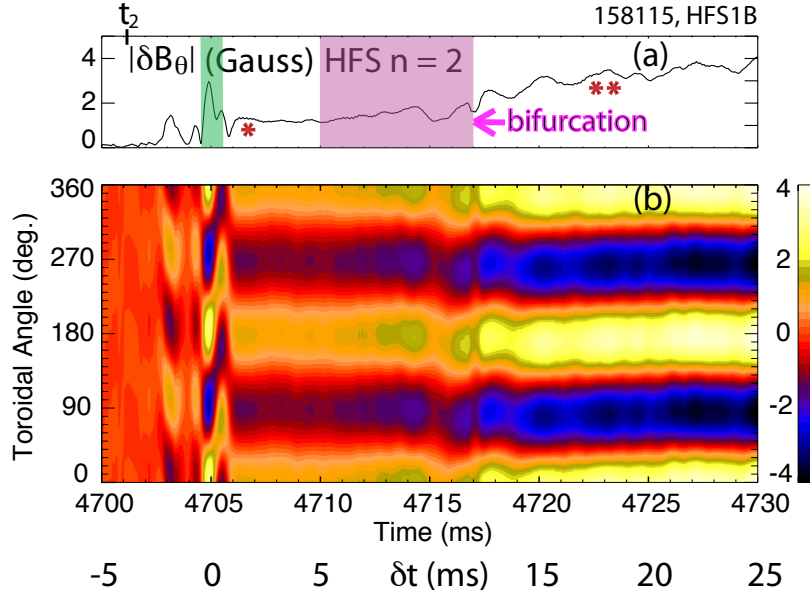


**Figure 7.** *Shortest time scale.* The measured HFS  $n = 2$  magnetic perturbation evolves on a short time scale: (a) amplitude of 3-D perturbed poloidal magnetic field  $|\delta B_\theta|$ ; (b) contour plot of the evolution of the toroidal phase angle of  $\delta B_\theta$ . The numbers in the color bar at the right represent the strength of  $\delta B_\theta$  in Gauss. The roughly linear increase in the Toroidal Angle (deg.) with time just after 4704.5 ms indicates this magnetic response during the ELM propagates with a toroidal rotation frequency of  $\omega_t^{\text{ELM}} \sim 2 \times 10^3 \text{ rad} \cdot \text{s}^{-1}$ . After 4706 ms the perturbation's toroidal angle is nearly constant in time which indicates the measured  $\delta B_\theta$  then locks to  $\omega_t^{\text{res}} \rightarrow 0$ , i.e., to the stationary laboratory (RMP) frame. Thereafter, this magnetic perturbation remains locked to the RMP frame as the pedestal bifurcates into ELM suppression during the  $\delta t = 5\text{--}12 \text{ ms}$  (4710–4717 ms) time interval and grows slowly\*\* thereafter.

magnitude  $B_{mn}^{\text{res}}(t) \equiv B_{mn}(\rho_{m/n}, t)$  there that is governed by

$$\frac{\partial B_{mn}^{\text{res}}}{\partial t} = \frac{C_{\text{ELM}} e^{i\omega t}}{\tau_{\text{SP}}} B_{mn}^{\text{ELM}}, \quad (10)$$

$$C_{\text{ELM}} \equiv \left( \rho_{m/n} \Delta'_{\text{RMP } m/n} \right)^{3/2} \frac{w_{\text{ELM}}}{4 \rho_{m/n}}. \quad (11)$$

This prediction is only valid for  $t \lesssim \tau_{\text{FKR}}$ , the Furth-Killeen-Rosenbluth growth time for linear tearing modes [31]; for longer times the thin nonlinearly driven resistive layer response decays [38] and the resultant much slower nonlinear evolution is determined by the modified Rutherford equation [30] described in section 8. Here,  $\tau_{\text{FKR}} \equiv S^{3/5} \tau_A / m^{4/5} \simeq 4 \times 10^{-4} \text{ s}$  and  $\tau_{\text{SP}} \equiv (mS)^{1/2} \tau_A \simeq 9 \times 10^{-4} \text{ s}$  is the Sweet-Parker time for abrupt externally driven magnetic reconnection. The reference island width the ideal perturbation  $B_{mn}^{\text{ELM}}$  would produce if it were a reconnected field there is  $w_{\text{ELM}} \equiv 4 [(L_{\text{sh}}/k\theta) (B_{mn}^{\text{ELM}}/B_{t0})]^{1/2}$ . Making a rough estimate from Fig. 7(a) of  $B_{82}^{\text{ELM}} \simeq 3 \text{ G}$  yields  $w_{\text{ELM}} \simeq 2.1 \text{ cm}$  and thus  $C_{\text{ELM}} \simeq 0.95$  at the 8/2 rational surface.

*Theory of ELM-crash-induced toroidal rotation.* The frequency  $\omega$  in (10) is caused by the toroidal motion of the ELM-crash-induced  $B_{mn}^{\text{ELM}}$  relative to the stationary

I-coils that produce the RMPs. During a P-B instability the relevant ideal MHD instability frequency is  $n = 2$  times the toroidal component of the equilibrium  $\mathbf{E}_0 \times \mathbf{B}_0 = -\mathbf{B}_0 \times \nabla \Phi_0$  velocity plus a small ion diamagnetic flow velocity which will be neglected for simplicity, i.e.,  $\omega_t^{\text{ELM}} \simeq n \Omega_E^{\text{ELM}}$  in which  $\Omega_E^{\text{ELM}} \equiv \nabla \zeta \cdot \mathbf{B}_0 \times \nabla \Phi_0 / B_0^2 = -(\psi_p'^2 / R^2 B_0^2) (d\Phi_0 / d\psi_p) = (B_p / R B_0^2) E_\rho \simeq \langle B_p^2 / B_{t0}^2 \rangle \omega_E$ . Since nonlinear ballooning modes in the pedestal continue to grow exponentially as an individual eigenmode well into the nonlinear regime [41], it will be assumed that P-B modes behave similarly and that  $\omega_E$  is roughly constant during the growth of the ELM. Using the maximum  $|\omega_E| \simeq 3 \times 10^4 \text{ rad} \cdot \text{s}^{-1}$  [see Fig. 4(c)] which occurs near the top half of the pedestal where the drive for the P-B instability eigenmode is likely centered and  $\langle B_p^2 / B_{t0}^2 \rangle \equiv \langle (\psi_p' / R B_0)^2 \rangle \simeq 0.02$  yields a prediction of  $\omega_t^{\text{ELM}} \simeq 1.2 \times 10^3 \text{ rad} \cdot \text{s}^{-1}$ . This result is reasonably close to the experimental  $\omega_t^{\text{ELM}} \simeq 2 \times 10^3 \text{ rad} \cdot \text{s}^{-1}$  that is inferred from Fig. 7(b) in the 4704.5–4705.5 ms time interval around  $\delta t = 0$ .

*Predicted ELM-crash-induced reconnection.* The reconnected resonant magnetic field  $B_{mn}^{\text{res}}$  that could be caused during the  $\delta t_{\text{ELM}} \lesssim 1$  ms ELM crash will be estimated assuming for simplicity that  $B_{82}^{\text{ELM}}$  is constant for at least the time  $\tau_{\text{FKR}} \simeq 0.4$  ms during the 4704.5–4705.5 ms time interval around  $\delta t = 0$ . Then, integrating (10) over time yields a reconnected magnetic field  $B_{mn}^{\text{res}}$  that grows linearly in time according to  $B_{mn}^{\text{res}}(t) \simeq (t/\tau_{\text{SP}}) C_{\text{ELM}} B_{mn}^{\text{ELM}}$ , up to the minimum of: 1) the  $\delta t_{\text{ELM}} \lesssim 1$  ms time interval, 2) the inverse of  $\omega \equiv \omega_t^{\text{ELM}}$  so the  $e^{i\omega t}$  in (10) is near unity and not oscillatory, and 3)  $\tau_{\text{FKR}}$  for applicability of (10). The time-asymptotic reconnected magnetic field strength on the 8/2 resonant surface induced by the ELM crash is thus predicted to be

$$B_{mn}^{\text{res}}(t) \simeq \frac{\min\{t, \tau_{\text{rec}}\}}{\tau_{\text{SP}}} C_{\text{ELM}} B_{mn}^{\text{ELM}}, \quad (12)$$

$$\tau_{\text{rec}} \simeq \min\{\delta t_{\text{ELM}}, 1/\omega_t^{\text{ELM}}, \tau_{\text{FKR}}\}. \quad (13)$$

Using the previously specified parameters  $\tau_{\text{SP}} \simeq 0.9$  ms and  $C_{\text{ELM}} \simeq 0.95$  at the 8/2 rational surface plus  $\tau_{\text{rec}} = \tau_{\text{FKR}} \simeq 0.4$  ms yields  $B_{82}^{\text{res}}(\tau_{\text{FKR}}) / B_{82}^{\text{ELM}} \simeq 0.4$ . This prediction agrees well with the reduction of  $|\delta B_\theta|$  from its maximum in the 4704.5–4705.5 ms interval around  $\delta t = 0$  to its value in the  $\delta t \simeq 1$ –5 ms (4706–4710 ms) time interval in Fig. 7(a). Using the estimate of  $B_{82}^{\text{res}}(\tau_{\text{FKR}}) \simeq 0.4 B_{82}^{\text{ELM}} \simeq 1.2$  G and (3) yields a “seed island” (like for NTMs) with initial width  $w_{\text{seed}} \equiv 4 [(L_{\text{sh}}/k_\theta) (B_{82}^{\text{res}}/B_{t0})]^{1/2} \simeq 1.3$  cm.

*Why does significant reconnection only occur at the 8/2 surface at  $t_3 = 4781$  ms?* The coefficient  $C_{\text{ELM}}$  represents the RMP drive for both the ELM-crash-induced reconnection discussed here and the evolution of the nonlinear island width discussed in section 8 that is applicable after the  $\delta t \simeq 1$ –5 ms (4706–4710 ms) transient phase (see section 7). This drive coefficient is likely to be smaller on the 7/2 and 9/2 surfaces for two reasons: 1)  $(\rho_{mn} \Delta'_{\text{RMP } m/n})^{3/2}$  will be smaller because kink responses near these adjacent rational surfaces are smaller [see Fig. 2(a)]; and 2)  $B_{72}^{\text{ELM}}$  is probably smaller because the P-B instability eigenmode is likely peaked outside the 8/2 surface and hence smaller on the 7/2 rational surface. Also, the lower  $T_e$  at the 9/2 surface reduces  $\tau_{\text{FKR}}$  and hence the predicted  $B_{92}^{\text{res}}$  and concomitant seed island width  $w_{9/2}^{\text{res}}$ . These effects

could reduce the predictions for the reconnected  $B_{mn}^{\text{res}}$  and seed island widths  $w_{m/n}^{\text{res}}$  on these adjacent surfaces. As discussed in section 8, smaller RMP drives and seed island widths in the modified Rutherford equation (17), which is applicable during and after the  $\delta t \simeq 5\text{--}12$  ms (4710–4717 ms) bifurcation period, should cause the tearing perturbations at the  $7/2$  and  $9/2$  surfaces to decay. This could explain why at  $t_3 = 4781$  ms, which is long after the bifurcation into ELM suppression, significant RMP-driven magnetic reconnection only occurs on the  $8/2$  rational surface in Fig. 2(b).

## 6. Plasma rotation and $E_\rho$ during an ELM crash

*Induced plasma torque and flutter transport.* As described in the preceding section, during the 1 ms time interval after the ELM begins to grow at 4704.5 ms, FMR theory predicts plasma resistivity causes the ideal MHD magnetic perturbation  $B_{mn}^{\text{ELM}}$  to induce the temporally growing resonant radial magnetic field  $B_{mn}^{\text{res}}$ . The plasma resistivity  $\eta$  causes it to also produce [28] a parallel (to  $\mathbf{B}_0$ ) current density  $\delta J_{\parallel m/n}^{\text{res}} \sim (T_e/e\eta) \int d^3v (v_{\parallel}/B_0) \delta \mathbf{B}_{m/n} \cdot \nabla f_{\text{Max}}$  in the  $\delta_\eta$  resistive layer around the rational surface. This dissipative parallel current is in phase with the radial magnetic perturbation  $B_{mn}^{\text{res}}$  that produces the radial magnetic flutter of magnetic field lines. The combination of these effects produces a radially local  $\delta \mathbf{J}_{\parallel m/n} \times \delta \mathbf{B}_{m/n}$  torque density on the plasma, which acts primarily in the poloidal ( $\theta$ ) direction [21, 28]:  $\tau_{e\theta} \equiv q\psi'_p \langle \overline{\delta J_{\parallel m/n}^{\text{res}} \delta \mathbf{B}_{m/n} \cdot \nabla \rho} / B_0 \rangle = -qRB_p e \Gamma_e^{\text{flutt}}$ . As indicated, the torque at a  $\rho_{m/n}$  rational surface is related to the (quasilinear) flutter-induced non-ambipolar radial electron density flux that is caused by these same effects [24, 28]:

$$\begin{aligned} \Gamma_e^{\text{flutt}}(\rho_{m/n}, t) &\equiv -n_e D_{et} \left[ \frac{d \ln p_e}{d\rho} + 0.71 \frac{d \ln T_e}{d\rho} + \frac{e}{T_e} E_\rho \right]_{\rho_{m/n}} \\ &= -(n_e e / T_e) D_{et}(\rho_{m/n}, t) R B_p \Omega_e^\alpha(\rho_{m/n}, t) \\ &\implies -(n_e e / T_e) D_{et}(\rho_{m/n}, t) E_\rho(\rho_{m/n}, t). \end{aligned} \quad (14)$$

Section 3 showed that flutter transport in the vicinity of the  $m/n$  rational surfaces relax the electron density and temperature gradients within the reconnection layers and thereby cause  $R B_p \Omega_e^\alpha$  to become simply  $E_\rho$  at the rational surfaces. This effect is taken into account in the last line of (14). This property continues to be applicable as  $B_{82}^{\text{res}}(\rho_{8/2}, t)$  grows in time.

*Procedure for determining  $E_\rho(t)$  at  $\rho_{8/2}$ .* The evolution of the radial electric field can be determined during the 4704.5–4705.5 ms time interval around  $\delta t = 0$  where the ideal magnetic perturbation  $B_{82}^{\text{ELM}}$  induces  $B_{82}^{\text{res}}(\rho_{8/2}, t)$  using the (nonlinear) poloidal torque balance. While the inertia term in the poloidal torque balance can be significant during the first 0.1 ms of growth of  $B_{82}^{\text{res}}(\rho_{8/2}, t)$ , it is negligible thereafter [24]. Thus, the evolution of the radial electric field can be determined by balancing the temporally growing flutter-induced transport and consequent torque against the ion torque that determined  $E_\rho$  before the ELM crash. That ion torque density will be modeled for the deuterium ions as [24, 29]  $\tau_{i\theta} = q R B_p e \Gamma_i^{na}$ , in which  $\Gamma_i^{na} = (n_i e / T_i) D_i^{na}(E_\rho - E_\rho^{\text{sym}})$ .

Here,  $D_i^{na}$  is a phenomenological non-ambipolar (superscript *na*) ion density diffusivity [29] in the pre-RMP transport equilibrium and  $E_\rho^{\text{sym}}$  is the radial electric field that existed in that near-axisymmetric (superscript *sym*) state. In cylindrical models of mode locking induced by field errors [16, 17],  $D_i^{na}$  is assumed to be caused by an anomalous perpendicular ion viscosity, and  $E_\rho$  and  $E_\rho^{\text{sym}}$  are replaced by cylindrical model versions of the corresponding toroidal flows inferred from  $\Omega_e^\alpha$  defined in (7). However, there can be a number of other effects that can contribute to the non-ambipolar ion density flux and ion flows [42], particularly in the pedestal region. For simplicity it will be assumed  $D_i^{na}$  and  $E_\rho^{\text{sym}}$  do not change significantly during the 4704.5-4705.5 ms ELM crash time interval around  $\delta t = 0$ .

*Prediction of  $E_\rho(t)$  during ELM crash.* Equating the electron flutter and ion torque densities yields an equation for the temporal evolution of the radial electric field [29]:

$$E_\rho(\rho_{8/2}, t) = \frac{E_\rho^{\text{sym}}}{\kappa(t) + 1}, \quad \kappa(t) \equiv \frac{n_e T_i}{n_i T_e} \frac{D_{\text{et}}(\rho_{8/2}, t)}{D_i^{na}}. \quad (15)$$

Here, the coefficient  $\kappa(t) \propto [B_{82}^{\text{res}}(\rho_{8/2}, t)]^2$  is a temporally growing measure of how large the RMP-induced poloidal torque, which is growing quadratically in time, is compared to the residual torque that determined  $E_\rho$  before the ELM crash. The non-ambipolar ion diffusivity will be assumed to be  $D_i^{na} = 0.35 \text{ m}^2 \cdot \text{s}^{-1}$ . This value is half the interpretively determined [26] (ambipolar) ion thermal diffusivity at the 8/2 surface of  $\chi_i \simeq 0.7 \text{ m}^2 \cdot \text{s}^{-1}$  at  $\delta t = -4$  ms (4701 ms), which is often dominantly due to the intrinsically ambipolar [43] neoclassical processes at this radius [26]. Further, using the previous sections' prediction of the ultimate ELM-crash-induced resonant field of  $B_{82}^{\text{res}}(\tau_{\text{FKR}}) \simeq 1.2$  G, the flutter radial diffusivity is  $D_{\text{et}}(\rho_{8/2}, \tau_{\text{FKR}}) \simeq 6 \text{ m}^2 \cdot \text{s}^{-1}$ . Together these assumptions yield  $\kappa(\tau_{\text{FKR}}) \sim 40 \gg 1$  at the final ELM-crash-induced state. Since  $\kappa$  is so large, the radial electric field  $E_\rho(\rho_{8/2})$  and hence the toroidal rotation frequency  $\Omega_E^\alpha(\rho_{8/2}) = \omega_E(\rho_{8/2}) = E_\rho(\rho_{8/2})/RB_p$  are predicted to be forced to zero for times greater than  $\tau_{\text{FKR}} \sim 0.4$  ms during the ELM crash. This is consistent with what is observed experimentally in Fig. 7(b) since the toroidal phase is stationary (i.e.,  $\omega_t^{\text{res}} \propto E_\rho \rightarrow 0$ ) after  $\delta t = 1$  ms (4706 ms).

*Mode-locked state.* Thus, during the about 1 ms ELM crash the substantial forced magnetic reconnection caused by the ideal MHD  $B_{82}^{\text{ELM}}$  at the 8/2 rational surface is predicted to produce the  $B_{82}^{\text{res}}(\rho_{8/2}, t)$  in (12) which in turn drives the radial electric field and electron fluid toroidal rotation to zero there — i.e., to a plasma state where  $\delta B_\theta$  is mode-locked to the stationary RMP coils in the  $\delta_\eta$  layer. This predicted state is analogous to the mode-locked state induced by field errors [16, 17]; however, it is different because here it is induced by the poloidal torque caused by the abrupt magnetic reconnection caused by the ELM crash instead of being caused by the slowly evolving effects of perpendicular ion viscosity on the toroidal plasma flow [16, 17]. The transition into a mode-locked state here is more analogous to how ELMs and sawteeth nonlinearly excite seed islands for NTMs [39, 40]; however, here the toroidal rotation frequency is relaxed to the stationary RMP rest frame rather than to the rotating frame of the NTM.

## 7. Initial tearing response stage

*Transient stage.* During the  $\delta t = 1\text{--}5$  ms (4706–4710 ms) time interval, the pedestal is predicted to be in a multi-faceted transient stage that is responding to the dramatic magnetic reconnection and plasma rotation changes at the  $8/2$  rational surface induced by the ELM crash during the preceding  $\sim 1$  ms time interval. Figure 7(b) shows the toroidally rotating, ELM-crash-induced ideal MHD perturbation  $B_{82}^{\text{ELM}}$  is not present during this period. The following paragraphs describe the primary physical processes that occur and their consequences during and slightly after this 4 ms period.

*Magnetic and  $E_\rho$  responses.* The ballooning-type  $n = 2$  P-B magnetic perturbation that is observed on the low field side (LFS) [14] decays with an exponential decay time of about 3 ms. But the extra\* HFS-measured  $n = 2$   $\delta B_\theta$  tearing-type perturbation is about constant during the  $\delta t = 1\text{--}5$  ms (4706–4710 ms) time interval for both the smallest and largest RMPs [see Fig. 6(c)]. In addition, since the experimental  $\omega_t^{\text{res}} \simeq 0$  and the predicted  $\Omega_E^\alpha(\rho_{8/2}) = \omega_E(\rho_{8/2}) = E_\rho(\rho_{8/2})/RB_p \simeq 0$ , both  $B_{82}^{\text{res}}$  and the electron fluid at the  $8/2$  rational surface remain mode-locked to the stationary RMPs.

*Radial diffusion of localized response caused by flutter transport.* The  $n_e$  and  $T_e$  profile flattening responses discussed in section 3 are predicted to be initially localized in the thin  $\delta_{\parallel t} \simeq 0.2$  cm layer around the magnetic island separatrix. However, during this  $\delta t = 1\text{--}5$  ms time interval they diffuse radially by flutter transport [29]. Assuming that  $B_{82}^{\text{res}} = 1.2$  G during this period and using (3), the initial island width is  $w_{\text{seed}} \simeq 1.3$  cm. Outside the  $\delta_{\parallel t}$  layer and magnetic island regions the equilibrium spatially-averaged radial transport is dominated by the minimum flutter diffusivity midway between two rational surfaces [28] [i.e., at  $\rho_{\text{mid}} \equiv (\rho_{m/n} + \rho_{m+1/n})/2$ ], where it can be written as [29]

$$D_{\text{et}}(\rho_{\text{mid}}) \simeq 0.5 (\nu_e \nu_{Te})^{1/2} (R_0 q)^{3/2} \left[ \frac{B_{mn}^2 + B_{m+1n}^2}{B_{t0}^2} \right]. \quad (16)$$

The  $B_{mn}$  amplitudes can be estimated midway between the  $7/2$  and  $8/2$  surfaces at  $\rho_{\text{mid}} \simeq 0.91a$  using profiles in Fig. 2(b) and  $B_{82}^{\text{res}} \simeq 1.2$  G, which yield  $B_{72}(\rho_{\text{mid}}) \simeq 0.6$  G and  $B_{82}(\rho_{\text{mid}}) \simeq 1.65$  G, and a flutter diffusivity  $D_{\text{et}}(\rho_{\text{mid}}) \simeq 0.09 \text{ m}^2 \cdot \text{s}^{-1}$ . Thus, during this  $\delta t_{\text{trans}} = 4$  ms the initially localized  $n_e$  and  $T_e$  responses diffuse radially a distance  $\delta \rho_{\text{trans}} \sim \sqrt{D_{\text{et}} \delta t_{\text{trans}}} \sim 2$  cm. Hence, during this transient stage flutter transport is predicted to diffuse the radially localized ELM crash effects almost to the adjacent rational surfaces at  $|\Delta_m| \sim 1/(nq') \sim 2.56$  cm or  $\delta \rho \sim 0.04 a \simeq 3.2$  cm from Fig. 2(b).

*Poloidal and toroidal ion flow theory.* During the  $\sim 1$  ms ELM crash around  $\delta t = 0$  the relevant torque balance was the poloidal one and it evolved into equilibrium during this short time. After about an ion collision time  $\tau_{ii} \sim 3$  ms the deuterium (subscript  $D$ ) poloidal flow is damped to its neoclassical equilibrium value  $q \mathbf{V}_D^{\text{nc}} \cdot \nabla \theta \simeq (1.17/e) (dT_D/d\psi_p)$  during which time the plasma's toroidal angular momentum is conserved [43]. Then, the longer time scale ion toroidal torque balance and toroidal ion flows  $\mathbf{V}_i \cdot \nabla \zeta$  become relevant [42]. The toroidal rotation frequency obtained from the radial force balance equation for any ion species (subscript  $i$ ) can be written as [42]  $\Omega_{it} \equiv \mathbf{V}_i \cdot \nabla \zeta \simeq [E_\rho - (n_i Z_i e)^{-1} (dp_i/d\rho)] / RB_p + q \mathbf{V}_i \cdot \nabla \theta$ . In the toroidal torque density

balance the flutter-induced non-ambipolar electron density flux induces a toroidal torque density  $\tau_{e\zeta}^{\text{flutt}} = RB_p e \Gamma_e^{\text{flutt}}$  that is usually in the co-current direction in the pedestal.

*Carbon flows.* No direct measurement of the poloidal and toroidal flows of the dominant deuterium ions are available for discharge 158115 in DIII-D. However, the CER system [36] provides such measurements for fully stripped carbon impurities in the pedestal. The carbon toroidal flow is  $V_{Ct} \simeq R \Omega_{Ct} \simeq [E_\rho - (6n_C e)^{-1}(dp_C/d\rho)]/RB_p + q\mathbf{V}_C \cdot \nabla\theta$ . During the equilibrium before bifurcation, Figs. 1, 5 and 6 show  $V_{Ct}$  is rather small, typically less than  $10 \text{ km} \cdot \text{s}^{-1}$ . Apparently the terms in  $V_{Ct}$  nearly cancel before bifurcation so  $E_\rho^{\text{sym}} \sim (6n_C e)^{-1}(dp_C/d\rho) \ll 0$ . However, as discussed in the preceding section, during the  $\sim 1$  ms ELM crash around  $\delta t = 0$  (4705 ms) the growing resonant field  $B_{mn}^{\text{res}}$  is predicted to create a large flutter-induced poloidal torque which the  $\kappa \gg 1$  limit of (15) indicates forces the negative  $E_\rho^{\text{sym}}$  at the 8/2 rational surface up to essentially zero. Then, during the  $\delta t = 1\text{--}5$  ms (4706–4710 ms) time interval and thereafter the initially localized change in  $V_{Ct}$  likely diffuses radially away from the 8/2 surface to the adjacent rational surfaces due to  $D_i^{\text{sym}}$ , analogous to the flutter-induced radial diffusion  $D_{et}$  effects discussed above. This process could be responsible for the apparently slightly delayed response\* observed in Figs. 5(b) and 6(b) of the carbon flow  $V_{Ct}$  in the top half of the pedestal (i.e., at normalized  $\psi_p \simeq 0.97$ ) to the change in  $\delta B_\theta$ . The later continued growth\*\* and eventual saturation of  $V_{Ct}$  at about  $35 \text{ km} \cdot \text{s}^{-1}$  in Fig. 5(b) could be due to the longer time scale evolution of the pedestal plasma parameters and coupling with core plasma changes. Perhaps the most important point here is that the evolution of the carbon flow in Figs. 5(b) and 6(b) is not predicted to be the cause of the magnetic reconnection on the rational surface. It is instead predicted to be a response to and thus delayed from the abrupt ( $\sim 1$  ms) ELM-crash-induced increase in the magnetic penetration and reconnection embodied in the increase in  $\delta B_\theta$  and  $B_{82}^{\text{res}}$ . This prediction can be tested in the future with faster CER data that has improved radial resolution by comparing it to the HFS magnetic response data.

## 8. Finally: bifurcation during and after $\delta t = 5\text{--}12$ ms (4710–4717 ms)

*Nonlinear response to RMP.* As shown in Fig. 6(c), the response to an ELM crash is roughly independent of the applied RMP amplitude up to about  $\delta t = 5$  ms (4710 ms). Further temporal evolution of  $|\delta B_\theta| \sim B_{82}^{\text{res}} \propto w^2$  is predicted by the nonlinear modified Rutherford equation (MRE) [30, 24] because the relevant island widths ( $w$ ) are larger than the total resistive layer width  $2\delta_\eta \simeq 0.3$  cm:

$$\dot{w} \equiv \frac{\partial w}{\partial t} \simeq D_\eta \left[ \Delta'_{8/2} + \Delta'_{\text{RMP } 8/2} \frac{w_{\text{vac}}^2}{w^2} - \frac{w_{\text{pol}}^2}{w^3} \right]. \quad (17)$$

Here, NTM effects [39, 40] and near unity numerical factors have been neglected for simplicity. The predicted behavior of the rate of growth of the magnetic island width ( $\dot{w}$ , in units of  $\text{cm} \cdot \text{s}^{-1}$ ) as a function of the island width is shown in Fig. 8.

*Specific parameters.* The parameters of the MRE in (17) for DIII-D discharge 158115 [14, 15] used to plot Fig. 8 are: effective magnetic diffusivity  $D_\eta \simeq 1400 \text{ cm}^2 \cdot \text{s}^{-1}$ ,

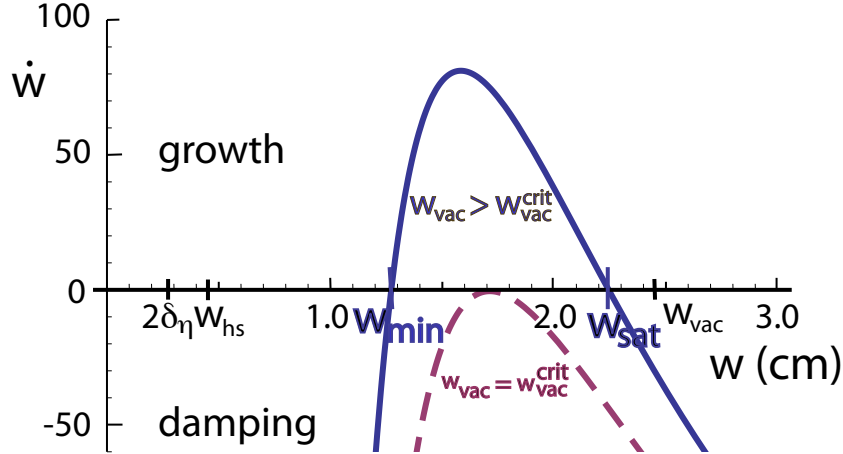


**Figure 8.** Growth ( $\dot{w} \equiv \partial w / \partial t > 0$  region of solid line) of a seed magnetic island of width  $w_{\text{seed}}$  is predicted by (17) if  $w_{\text{min}} < w_{\text{seed}} < w_{\text{sat}}$ . The island width decays for  $w < w_{\text{min}}$  mainly because of the ion banana width polarization current effects and for  $w > w_{\text{sat}}$  mainly due to the negative tearing mode stability index  $\rho_{8/2} \Delta'_{8/2} \simeq -16 < 0$ . The dashed curve is for marginal stability which occurs when the vacuum island width is reduced from 2.45 to 2.3 cm or  $\rho_{8/2} \Delta'_{\text{RMP } 8/2}$  is reduced from 26.4 to 23.3. Thus, only a small increase in the RMP drive ( $\rho_{8/2} \Delta'_{\text{RMP } 8/2}$ )  $w_{\text{vac}}^2$  in (17) is needed to change from marginal stability to possible temporal growth of  $w$  for a  $w_{\text{seed}} > w_{\text{min}}$  seed island.

tearing stability index  $\rho_{8/2} \Delta'_{8/2} \simeq -2m = -16$ , RMP-induced island growth factor for the  $B_{82}$  model in (1) defined in (5)  $\rho_{8/2} \Delta'_{\text{RMP } 8/2} \simeq 26.4$ , RMP-induced vacuum island width  $w_{\text{vac}} \equiv 4 [(L_{\text{sh}}/k_{\theta}) (B_{82}^{\text{vac}}(\rho_{8/2})/B_0)]^{1/2} \simeq 2.45$  cm, and  $w_{\text{pol}} \simeq 1.5$  cm. Here,  $w_{\text{pol}}$  represents ion polarization current effects [44, 45, 46]. In experimental studies of NTM threshold island widths [47, 48, 49] it is parameterized in terms of the ion banana width parameter  $w_{\text{ib}} \equiv q \varrho_i / \sqrt{\epsilon} \simeq 3$  cm in terms of which it can be written as  $w_{\text{pol}} \equiv C_{\text{pol}} w_{\text{ib}}$ . The numerical coefficient here scales as  $C_{\text{pol}}^2 \sim \beta_{\theta} (\rho_{m/n} / \hat{s} L_P)^2 f_{\text{pol}}(\omega, \nu_i / \epsilon)$ . An empirical value of  $C_{\text{pol}} \simeq 1.9$  provides reasonable characterizations for determining minimum seed island widths for growth of NTMs in many tokamaks [47], although  $C_{\text{pol}} \simeq 1.3$  is more appropriate for NTMs at large  $\rho_{2/1}$  in DIII-D [48, 49]. Because  $\beta_{\theta}$  and  $(\rho_{m/n} / \hat{s} L_P)^2$  are smaller at the top of the pedestal, a value of  $C_{\text{pol}} = 0.5$  is assumed here.

*Damped responses in MRE.* Figure 8 shows that if the seed island is too small (i.e.,  $w_{\text{seed}} < w_{\text{min}}$ ), the  $w_{\text{pol}}$  ion polarization current effects in (17) cause the island width  $w$  and hence  $B_{mn}^{\text{res}} \propto |\delta B_{\theta}|$  to be damped. This prediction can apparently explain why the smallest applied RMP case shown by the gray line for  $|\delta B_{\theta}|$  in Fig. 6(c) decays after about  $\delta t = 10$  ms (at  $4713 - 398 = 4315$  ms). It also provides a plausible explanation for why all the high slip strongly flow-screened states which have seed islands with  $w_{\text{seed}} \simeq w_{\text{hs}} \ll w_{\text{min}}$  are damped. Thus, it suggests that high slip states are not likely to be able to grow “out of the noise” into low slip states with large magnetic islands — unless, as discussed in section 3, the flow screening frequency at the 8/2 rational surface is exceedingly small [i.e.,  $|\omega_E(\rho_{8/2})| \lesssim 0.6$  krad $\cdot$ s $^{-1}$ ] for a fairly long time ( $> \tau_{\delta} \simeq 14$  ms). Instead, as proposed in this paper, in DIII-D discharge 158115 an ELM crash abruptly produces an 8/2 seed island with  $w_{\text{seed}} > w_{\text{min}}$ .

*Growth of ELM-crash-induced seed island.* Figure 8 shows an 8/2 magnetic island can grow if the seed island width  $w_{\text{seed}}$  exceeds  $w_{\text{min}}$  so RMP effects are large enough in (17) to produce  $\dot{w} > 0$ . The ELM-crash-induced seed island width predicted in section 5 is  $w_{\text{seed}} \simeq 1.3$  cm, which is perhaps fortuitously slightly greater than  $w_{\text{min}} \simeq 1.28$  cm in Fig. 8. As described below, the growth of the island width  $w(t)$  predicted by integrating (17) over time after the transient stage [i.e., after  $\delta t = 5$  ms (4710 ms)] approximately reproduces the slow growth\*\* of  $|\delta B_\theta(t)| \propto w(t)^2$ , as shown in Fig. 6(c).

*Critical condition for island growth.* The minimum  $w_{\text{vac}}$  required for the 8/2 island width to grow in time is predicted from the condition that the three solutions of the cubic equation for  $w$  obtained from the equation  $\dot{w} = 0$  are real:

$$w_{\text{vac}} > w_{\text{vac}}^{\text{crit}} \equiv w_{\text{pol}}^{2/3} \rho_{8/2}^{1/3} \frac{[(27/4) |\rho_{8/2} \Delta'_{8/2}|]^{1/6}}{[\rho_{8/2} \Delta'_{\text{RMP } 8/2}]^{1/2}},$$

critical vacuum island width for growth. (18)

When this condition is satisfied, a seed island with  $w_{\text{seed}} > w_{\text{min}}$  is predicted to grow temporally from  $w_{\text{seed}}$  up to  $w_{\text{sat}}$ . During this time  $B_{82}^{\text{res}}(t) \propto [w(t)]^2$  can apparently produce sufficient flutter-induced electron transport to reduce the pedestal top  $n_e$  and  $T_e$  gradients enough to suppress P-B instabilities (see next section). Thus, the criterion in (18) will become the fundamental theoretical prediction for how large externally imposed RMPs must be to produce ELM suppression in these  $n = 2$  DIII-D experiments [14, 15]. Its primary scaling with various parameters and limitations are discussed in section 10.

*Comparisons with DIII-D experimental data.* For parameters used in this paper the critical RMP-vacuum-induced parameter in (18) is  $w_{\text{vac}}^{\text{crit}} \simeq 2.3$  cm. This value is slightly smaller than the  $w_{\text{vac}} \simeq 2.45$  cm inferred from the 8/2 response in Fig. 2(b). Thus, Fig. 8 predicts the 8/2 island width grows from  $w_{\text{seed}} \simeq 1.3$  cm up to  $w_{\text{sat}} \simeq 2.24$  cm. Figure 3(d) shows the magnetic field structure for a nearly equal low slip saturated island width  $w_{\text{ls}} \simeq 2.2$  cm. The time  $t$  after the transient stage for the island width to reach a given value is determined by integrating (numerically) the reciprocal of  $\dot{w}$  defined in (17) over  $w$  from  $w_{\text{seed}}$  to  $w(t)$ :  $t \equiv \int_{w_{\text{seed}}}^{w(t)} dw'/\dot{w}(w')$ . The inverse of this relation yields  $w(t)$  which implies temporal growth of  $B_{82}^{\text{res}}(t) = [k_\theta w(t)^2/16L_{\text{sh}}] B_{t0}$ . It will be assumed that for the largest applied RMP the predicted  $\delta B_\theta^{\text{pred}}(t) \simeq B_{82}^{\text{res}}(t)$ . This  $\delta B_\theta^{\text{pred}}(t)$  prediction is shown by the blue dots and connecting lines in Fig. 6(c) after  $\delta t = 5$  ms (4710 ms), which is in good agreement with the observed HFS  $n = 2$   $\delta B_\theta(t)$  there. For the minimum applied RMP at  $t_0 \simeq 4300$  ms,  $w_{\text{vac}}^2$  is negligible in (17). Then, the  $\delta B_\theta(t)$  decay can be estimated from  $t_{\text{decay}} \simeq B_{82}^{\text{res}}[t(w_{\text{seed}})] / |\dot{B}_{82}^{\text{res}}|_{w_{\text{seed}}} \simeq w_{\text{seed}}^4 / (2 D_\eta w_{\text{pol}}^2) \simeq 0.5$  ms, which is only a factor of two shorter than the  $\sim 1$  ms initial decay time of the  $\delta B_\theta$  gray curve after  $\delta t = 9$  ms (4316 ms) in Fig. 6(c).

*Near threshold conditions.* It is important to note that the situation being considered here is just marginally in the  $\dot{w} > 0$  island growth regime because  $w_{\text{vac}} \simeq 2.45$  cm is only slightly greater than  $w_{\text{vac}}^{\text{crit}} \simeq 2.3$  cm, which corresponds to an I-coil current of about 3.5 kA. This near threshold regime for RMP ELM suppression was fortuitously obtained in DIII-D discharge 158115 [14, 15] because the 4 kA I-coil current used there was operationally the maximum available in those  $n = 2$  experiments.

## 9. RMP-induced flutter transport

*RMP-induced plasma transport effects.* The changes in plasma transport and resultant changes in the plasma profiles in the pedestal caused by RMPs both before and after ELM suppression will now be considered. Figure 1(c) shows the pedestal top electron density  $n_{e,\text{ped}}$  decreases modestly as the strength of the RMPs and hence  $|\delta B_\theta|$  increases. During ELM suppression  $n_{e,\text{ped}}$  decreases more and  $T_{e,\text{ped}}$  decreases a bit. Figure 4 shows the changes in the profiles of various key parameters from just before ELM suppression (at  $t_2 = 4701$  ms) to the saturated state during ELM suppression (at  $t_3 = 4781$  ms). The key issues to be addressed in this section are: 1) what transport processes cause these effects?; 2) why is  $n_{e,\text{ped}}$  reduced more than  $T_{e,\text{ped}}$  before suppression? (i.e., what causes density “pump-out,” the reduction in pedestal density caused by RMPs?); 3) what causes the reductions in  $n_{e,\text{ped}}$  and  $T_{e,\text{ped}}$  during suppression?; and 4) how do flutter transport diffusivity predictions compare to diffusivities obtained from interpretive transport modeling [26] in DIII-D discharge 158115 [14, 15]?

*Magnetic island does not produce sharply defined  $T_e$ ,  $n_e$  islands.* As a magnetic island is being formed and grows the local parallel current density per unit magnetic field strength  $J_\parallel/B_0$  is forced to be constant on the  $\Psi_*$  helical flux surfaces discussed in section 2 on the very short shear-Alfvén time scale ( $\sim \mu\text{s}$ ) [24]. Thus, the magnetic island structures derived from the  $\Psi_* = \text{constant}$  surfaces shown in Fig. 3 are applicable throughout the magnetic island formation and growth. In contrast, the  $n_e$  and  $T_e$  profiles respond via the plasma transport processes parallel and perpendicular to the local magnetic field  $\mathbf{B} = \mathbf{B}_0 + \delta\mathbf{B}_{m/n}$ . In an asymptotic limit where parallel transport processes are infinitely large, both  $n_e$  and  $T_e$  also become functions of  $\Psi_*$  and hence constant on the magnetic field lines and island structures shown in Fig. 3. However,  $T_e$  is no longer constant on magnetic field lines when parallel transport is not infinite and perpendicular transport is present [50, 24]. For a relevant parallel electron thermal diffusivity of  $\chi_{e\parallel} \simeq 1.6 v_{Te}^2/\nu_{e\text{eff}} \simeq 3 \times 10^9 \text{ m}^2 \cdot \text{s}^{-1}$  and perpendicular diffusivity of  $\chi_{e\perp} \sim 2 \text{ m}^2 \cdot \text{s}^{-1}$  at  $t_3 = 4781$  ms, the perpendicular and parallel scale lengths on which  $T_e$  is not constant along a magnetic field line are [50, 24]  $x_{cT} \sim (L_{\text{sh}}/k_\theta)^{1/2} (\chi_{e\perp}/\chi_{e\parallel})^{1/4} \sim 0.2$  cm and  $L_{cT} \sim L_{\text{sh}}/(k_\theta x_{cT}) \sim 86$  m. The effective parallel thermal diffusivity length  $L_{cT}$  and the field line periodicity lengths  $L_\parallel$  for flutter and  $L_w$  within islands discussed in section 2 are all of the order of or longer than the effective electron collision length  $\lambda_{e\text{eff}} \equiv (f_c B_{\text{max}}/B_0) v_{Te}/\nu_e \sim 90$  m. Also,  $2x_{cT} \simeq 0.4$  cm is a significant fraction of the relevant half-island widths  $w/2$ . Thus,  $T_e$  is predicted to not be constant on field lines inside the magnetic island structures in Fig. 3, although  $T_e(\mathbf{x})$  may reflect the island structure to some degree. For the corresponding density diffusivity coefficients, the value of  $x_{cn}$  is a factor of order 4 larger and  $2x_{cn} \simeq 1.6$  cm is larger than the half-island width  $w/2 \simeq 1.1$  cm in Fig. 3(d). Thus, the  $n_e(\mathbf{x})$  profile is predicted to hardly reflect the magnetic island structure at all. No theoretical model has been developed for determining  $n_e$  and  $T_e$  transport across magnetic field lines in this parameter regime. However, since the radial magnetic flutter of field lines both

inside and outside of magnetic islands in Fig. 3 are similar, and  $n_e$  and  $T_e$  are not predicted to be constant along field lines, the flutter transport model [28, 29] should be reasonably appropriate. Thus, it will be used to estimate the radial electron transport fluxes relative to the equilibrium poloidal magnetic flux surfaces (i.e.,  $\psi_p$ ).

*Radial variation of flutter transport.* Radial electron density and heat transport induced by magnetic flutter across flux surfaces is very inhomogeneous [28, 29, 51, 52]. Flutter transport is quite large in the thin layers  $\delta_{\parallel t} \gtrsim \delta_\eta$  around rational surfaces [13, 23, 28, 52]. Section 3 discussed how it flattens the  $n_e$  and  $T_e$  gradients at rational surfaces, thereby causing the electron fluid flow frequency to only depend on  $E_\rho$  in the thin reconnection layers. Also, in section 6 the predicted ELM-crash-induced large increase in  $B_{82}^{\text{res}}$  and consequent increase in flutter transport and hence  $\delta \mathbf{J} \times \delta \mathbf{B}$  poloidal torque was shown to force  $E_\rho$  to zero on the 8/2 surface. However, flutter transport is much smaller between rational surfaces, because of magnetic shear effects [28]. As described in section 7, the radially-averaged flutter transport between rational surfaces is dominated by the minimum flutter diffusivity midway between two rational surfaces, which is defined in (16) [29].

*Flutter diffusivity effects in high slip state.* As section 7 indicates, in the high slip strongly flow-screened equilibrium before ELM suppression the predicted  $D_{\text{et}}(\rho_{\text{mid}}) \simeq 0.09 \text{ m}^2 \cdot \text{s}^{-1}$  is rather small. However, in a similar DIII-D H-mode plasma [26] the effective density diffusivity in the top half of the pedestal ( $0.94 < \rho_N < 0.98$ ) was shown to be rather small ( $D_{\text{eff}} \sim 0.02\text{--}0.1 \text{ m}^2 \cdot \text{s}^{-1}$ ) while the electron thermal diffusivity was much larger there ( $\chi_e \sim 0.3\text{--}0.8 \text{ m}^2 \cdot \text{s}^{-1}$ ). Thus, in the top half of the pedestal where the flutter diffusivity would be somewhat smaller than  $D_{\text{et}}(\rho_{\text{mid}}) \simeq 0.09 \text{ m}^2 \cdot \text{s}^{-1}$ , presuming this pedestal has similar properties to that in [26], flutter transport could apparently produce some density pump-out  $\propto \delta B_\theta^2$  without having much effect on  $T_{e,\text{ped}}$ .

*Flutter diffusivity in low slip state.* The magnetic perturbations at the midpoint between the 7/2 and 8/2 surfaces ( $\rho_{\text{mid}} \simeq 0.91a$ ) at  $t_3 = 4781$  ms can be estimated by multiplying their values in Fig. 2(b) by 4 kA, which yields  $B_{72}(0.91a) \simeq 1.6$  G and  $B_{82}(0.91a) \simeq 4.6$  G. Using (16) these estimates produce a flutter diffusivity of  $D_{\text{et}}(0.91a) \simeq 0.7 \text{ m}^2 \cdot \text{s}^{-1}$ . This yields a prediction (see Figs. 2 and 3 in [29]) for the radially-averaged average flutter-induced electron thermal diffusivity of  $\chi_e^{\text{flutt}}(0.91a) \sim 2 D_{\text{et}}(0.91a) \simeq 1.4 \text{ m}^2 \cdot \text{s}^{-1}$ . Before ELM suppression (i.e., at  $t_2 = 4701$  ms) the electron thermal diffusivity determined in the usual way from interpretive transport modeling [26] is  $\chi_e^{\text{sym}}(0.91a) \simeq 0.4 \text{ m}^2 \cdot \text{s}^{-1}$ . Assuming this ‘‘symmetric background’’  $\chi_e^{\text{sym}}$  does not change much during RMP ELM suppression, these diffusivities can be added to yield a predicted total electron thermal diffusivity during RMP ELM suppression of  $\chi_e^{\text{RMP}}(0.91a) \simeq \chi_e^{\text{sym}}(0.91a) + \chi_e^{\text{flutt}}(0.91a) \simeq 1.8 \text{ m}^2 \cdot \text{s}^{-1}$ . This prediction is in good agreement with the interpretively determined [26]  $\chi_e^{\text{sat}}(0.91a) \simeq 1.7 \text{ m}^2 \cdot \text{s}^{-1}$  in the saturated ELM suppressed state at  $t_3 = 4781$  ms. Thus, the flutter-induced transport caused by RMPs in the ELM suppressed state plausibly provides the additional electron transport responsible for the observed flattening of the  $T_e$  and  $n_e$  profiles in the key region ( $0.9 < \rho_N < 0.95$ , normalized  $\psi_p$  from 0.91 to 0.96) of Figs. 4(a) and 4(b).

*Possible fluctuation-induced transport.* Long wavelength ( $k_{\perp} \rho_i \simeq 0.5$ ) density fluctuations measured by BES at normalized  $\psi_p \simeq 0.94$  about doubled from before to during RMP ELM suppression in DIII-D discharge 158115 [15]. Shorter wavelength fluctuation levels might also change. The anomalous transport changes caused by these fluctuations could affect  $\chi_e^{\text{sym}}$  and increase transport during ELM suppression. Detailed modeling of plasma microturbulence and the anomalous  $T_e$ ,  $n_e$  and non-ambipolar electron transport it induces is needed for both the low slip and high slip states to ascertain how significant these effects could be. However, since the additional transport caused by magnetic flutter plausibly provides about the right amount of additional transport during RMP ELM suppression, perhaps any additional fluctuation-induced transport is not too important in the ELM suppressed state at  $t_3 = 4781$  ms.

*Qualitative trends of flutter transport effects.* During the equilibrium phase before ELM suppression in Fig. 1(c),  $n_{e,\text{ped}}$  decreases as  $\delta B_{\theta}$  increases — perhaps roughly as  $\delta B_{\theta}^2$ , as would be predicted by the flutter diffusivity  $D_{et} \propto \delta B_{\theta}^2$ . Thus, the  $n_{e,\text{ped}}$  density pump-out in this phase could be due primarily to the additional flutter density transport in the top half of the pedestal, without affecting  $T_{e,\text{ped}}$  much. During ELM suppression the additional flutter-induced  $T_e$  and  $n_e$  transport at the pedestal top is plausibly the dominant effect causing the reduction in the  $T_e$  and  $n_e$  gradients there that is necessary for stabilizing P-B modes and thereby suppressing ELMs [53]; some fluctuation-induced transport could contribute as well. Thus, the trends in the temporal behavior of the pedestal top  $n_{e,\text{ped}}$  and  $T_{e,\text{ped}}$  in Fig. 1(c), and  $T_e$  and  $n_e$  profile changes in the pedestal top region (normalized  $\psi_p$  between 0.91 and 0.96) in Figs. 4(a) and 4(b) from  $t_2 = 4701$  ms to  $t_3 = 4781$  ms are qualitatively consistent with the predictions of flutter transport.

## 10. Discussion of ELM-crash-induced RMP ELM suppression model

*Model overview.* The preceding sections provided many encouraging comparisons of DIII-D discharge 158115 [14, 15] data with predictions of the comprehensive model developed for it here. The key new feature of this multi-faceted model is that an ELM crash precipitates a sequence of events that ultimately lead to ELM suppression if the RMP applied at the 8/2 rational surface is large enough. Since there are a number of assumptions, approximations and data analysis limitations in the development of this model and its comparison to DIII-D data, this new model should not be regarded as definitively proven. Nonetheless, this section discusses the model presuming it provides a reasonable framework for describing RMP ELM suppression in DIII-D discharge 158115 [14, 15]. In so doing it highlights the logical progression of the model's key physics elements and comments on its major approximations and possible extrapolations. This section concludes with a discussion of how this model's predictions compare to other published type I RMP ELM suppression criteria [53, 54].

*Initial, ELMing equilibrium state of pedestal.* When edge-resonant magnetic field perturbations are added to an otherwise axisymmetric tokamak the pedestal plasma is metastable with two possible states: a high slip one with large flow-screening of the

RMPs at rational surfaces and little magnetic reconnection there, the other a low slip one with little or no flow-screening at a rational surface and significant reconnection that produces a moderate width magnetic island there. The behavior of a 3-D magnetic perturbation in a plasma is governed by Faraday's law with a perturbed electric field [16, 17, 24]. In the absence of plasma resistivity the radial magnetic perturbation is frozen into the electron fluid and rotates perpendicular to the helical magnetic field  $\mathbf{B}_{\text{hel}}$  in a flux surface with the frequency  $\Omega_e^\alpha \simeq \omega_{\perp e}$  defined in (7), which includes both  $\mathbf{E} \times \mathbf{B}$  and electron diamagnetic flows. However, plasma resistivity effects violate the frozen flux theorem in the very thin reconnection layer  $\delta_\eta$  around a  $q = m/n$  rational surface and some reconnection occurs there. The small amplitude of this resistivity-induced magnetic perturbation at a rational surface is sufficient for the (quasilinear) magnetic flutter transport it induces to remove the electron pressure-gradient-driven diamagnetic flow in the reconnection layer and cause the electron flow frequency to only depend on the radial electric field there, i.e.,  $\Omega_e^\alpha \simeq \omega_{\perp e} \rightarrow \omega_E$  as indicated in (9). Macroscopically this means the relevant frequency for flow screening is determined by the  $E_\rho$  obtained from the carbon impurity ion profiles, even as the electron pressure gradient outside the thin reconnection layer is unchanged. A key criterion for the applicability of this analysis is that the effective electron collision frequency  $\nu_{e\text{eff}} = \nu_e / (f_c B_{\text{max}} / B_{t0}) \simeq 3 \nu_e$  must be larger than  $n \Omega_e^\alpha \simeq 2 \omega_{\perp e}$  so flutter transport is dominantly dissipative [24, 28]. Perpendicular electron flow screens and hence reduces the radial component of the RMP below its vacuum value on rational surfaces by the factor  $f_{\text{scr}}$  defined in (4). In the equilibrium before ELM suppression, flow screening is very strong with little resistivity-induced reconnection at rational surfaces which produces small magnetic island widths of order the reconnection layer widths, as illustrated in Figs. 2(a), 3(a) and 3(b).

*ELM crash induces magnetic reconnection and RMP-locked perturbations.* An ELM crash abruptly precipitates the transition into the 8/2 RMP-penetrated, low slip, nonlinear magnetic island state where the seed island width  $w_{\text{seed}}$  is much larger than the reconnection layer width  $\delta_\eta$ . An ELM crash is caused by an ideal MHD P-B instability, whose nonlinear evolution produces many 3-D ideal MHD perturbations. The resonant ideal MHD perturbations cause rapidly growing forced magnetic reconnection at rational surfaces (up to the RMP vacuum level in  $\lesssim 1$  ms), as described by (10)–(13). This  $B_{mn}^{\text{res}}$  resonant perturbation produces a seed island of width  $w_{\text{seed}}$ . As the reconnected field strength increases at a rational surface, which is now the 8/2 magnetic island separatrix, the quasilinear magnetic flutter transport it induces has two important effects in the  $\delta_\eta$  reconnecting layers [see Fig. 3(d)]: 1) the radial electric field  $E_\rho$ , which is determined from the poloidal torque balance, is forced to zero there as indicated in (15); and 2) hence, as shown in Fig. 7(b), the toroidal rotation frequency of the  $n = 2$  magnetic perturbations is forced to zero. This means these  $n = 2$  magnetic perturbations become locked to the stationary RMP frame at the rational surfaces. There are two key applicability criteria for these ELM-crash-induced effects. First, the ELM crash and the reconnected perturbation it induces at the 8/2 surface must be large enough to produce a seed island that satisfies  $w_{\text{seed}} > w_{\text{min}}$  in Fig. 8. Equations (10)–(13) show the

reconnected  $B_{mn}^{\text{res}}$  is proportional to the product of the ELM-induced factor  $(B_{mn}^{\text{ELM}})^{3/2}$  and the RMP drive parameter  $\rho_{m/n}\Delta'_{\text{RMP } m/n}$  defined in (5). The RMP drive parameter is apparently largest in the region where kink-type  $B_{mn}$  responses are largest, perhaps in the  $0.9 < \rho_N < 0.96$  region where the edge bootstrap current gradient is positive and largest. Second, the amount of reconnection caused by the ELM crash must be sufficient for  $\kappa(t)$  in (15) to be large enough to force  $E_\rho$  to zero. While  $\kappa(\tau_{\text{FKR}}) \simeq 40 \gg 1$  is sufficiently large for the parameters used in modeling DIII-D discharge 158115, it could become smaller if  $B_{mn}^{\text{res}}$  was smaller than the assumed 1.2 G or if the electron flow frequency  $\Omega_e^\alpha$  at the  $m/n$  rational surface was large enough to cause  $D_{\text{et}}(\rho_{m/n})$  to be reduced by a factor  $[\nu_{e\text{eff}}/(n\Omega_e^\alpha)]^2$ , as described in section 3.

*Bifurcation into ELM suppressed state.* Immediately after the ELM-crash-induced strong magnetic reconnection stage the pedestal is in a roughly 4 ms transition phase where many new physical processes are important: the  $n = 2$  LFS ballooning responses decay, flutter transport diffuses the responses away from their initially radially localized responses, and neoclassical poloidal flow damping relaxes the poloidal ion flow. After these transient processes decay, the plasma's toroidal torque balance [42] becomes applicable and the temporal evolution of the seed island is governed by the nonlinear modified Rutherford equation given in (17) whose behavior is illustrated in Fig. 8. The 8/2 seed island then predictably decays (for a small applied RMP) or grows (for the largest applied RMP), as shown in Fig. 6(c). The ultimate criterion for the minimum RMP amplitude required for island growth and hence ELM suppression is given in (18):  $w_{\text{vac}} > w_{\text{vac}}^{\text{crit}}$  in which  $w_{\text{vac}} \propto B_{82}^{\text{vac}}(\rho_{8/2})^{1/2}$ , i.e., the square root of the I-coil current. The main conditions for this key result to be appropriate are those needed for the nonlinear modified Rutherford equation in (17) to be applicable: 1) the ELM-crash-induced 8/2 seed island width must be much larger than the resistive layer width  $2\delta_\eta$ ; 2) the 8/2 resonant perturbation must become mode-locked to the stationary RMPs; and 3) most importantly, the externally applied RMP must be large enough so (18) is satisfied. This last condition is effectively the ultimate criterion for how large the RMPs must be for ELM suppression because, as described in section 10, for the  $B_{mn}(\rho_{\text{mid}})$  values used here magnetic flutter transport can reduce the electron  $T_e$  and  $n_e$  gradients at the pedestal top enough to stabilize the P-B modes. The  $w_{\text{vac}}^{\text{crit}}$  parameter defined in (18) is proportional to the polarization-current-induced parameter  $w_{\text{pol}}$  to the 2/3 power and the RMP drive parameter  $\rho_{m/n}\Delta'_{\text{RMP } m/n}$ . As indicated in the preceding paragraph, the RMP drive parameter  $\rho_{m/n}\Delta'_{\text{RMP } m/n}$  is apparently largest where the bootstrap-current-gradient effects and kink-type  $B_{mn}$  responses are largest. In larger devices such as ITER the poloidal ion banana width would be a much smaller fraction of the minor radius ( $w_{\text{pol}}/a \sim w_{\text{ib}}/a \propto \varrho_i/a \equiv \varrho_{i*} \ll 1$ ), which should allow the ultimate criterion in (18) to be satisfied by a smaller  $B_{mn}^{\text{vac}}/B_{t0} \propto (w_{\text{pol}}/a)^{4/3} \propto \varrho_{i*}^{4/3}$ , i.e., less I-coil current.

*Model sensitivities and their implications.* If the RMP-inducing I-coil current is increased even slightly, the predicted island width growth time  $\tau_w \sim w/\max\{\dot{w}\} \sim 20$  ms for Fig. 6(c) decreases dramatically. For example, if the I-coil current increases from 4 to 5 kA, while the vacuum island width  $w_{\text{vac}}$  only increases by 12 %, the peak of  $\dot{w}$  occurs

at  $w \simeq 1.28$  cm where it is  $460 \text{ cm} \cdot \text{s}^{-1}$ , and the predicted  $\tau_w \simeq 2.8$  ms is almost an order of magnitude shorter. The parameter sensitivity of this ELM-crash-induced ELM suppression model could help explain why robust RMP ELM suppression in DIII-D is obtained for only a slight increase of the I-coil current above a minimum threshold [5]. A general criterion for applicability of the flutter transport model is that the  $T_e$  profile flattening width  $\delta_{\parallel t}$  must be small compared to the distance between rational surfaces [29], which requires  $\nu_{*e} \ll 1.2$  for DIII-D. This is well satisfied in discharge 158115 where  $\nu_{*e} \simeq 0.15$ . Finally, it can be speculated that the narrow  $q_{95}$  windows where RMP ELM suppression occurs [55, 56] might be centered near where  $\rho_{8/2} \Delta'_{\text{RMP } 8/2}$  is largest.

*Relation to vacuum island overlap criterion* [54]. An initial hypothesis for how large RMPs needed to be to obtain ELM suppression [2]–[5] was that the vacuum magnetic islands caused by multiple RMPs would overlap and produce magnetic stochasticity. This would induce stochasticity-driven transport [57] and reduce the pressure gradient in the edge, thereby stabilizing the P-B modes. And satisfaction of the Chirikov vacuum-island-overlap criterion from the separatrix in to a normalized radius of about 0.85 provides a useful empirical criterion [54] for the RMP field strength required for ELM suppression in low collisionality DIII-D plasmas. In terms of the parameters in this paper, this vacuum island overlap width (VIOW) criterion for RMP ELM suppression is roughly that the RMP-induced vacuum island width needs to be greater than the distance between rational surfaces, i.e.,  $w_{\text{vac}}^{\text{VIOW}} > 1/\Delta_m \simeq 1/nq'$ . For the DIII-D discharge 158115 parameters [14, 15] this yields a VIOW criterion of  $w_{\text{vac}}^{\text{VIOW}} \gtrsim 2.56$  cm, which is perhaps fortuitously close to the  $w_{\text{vac}} > w_{\text{vac}}^{\text{crit}} \simeq 2.3$  cm criterion in (18) for this new model. However, the scalings of the two models are very different. In particular, for ITER parameters where the poloidal ion banana width would be a much smaller fraction of the minor radius, the ultimate criterion for ELM suppression in (18), which implies  $w_{\text{vac}}^{\text{crit}}/a \propto (w_{\text{ib}}/a)^{2/3} \propto \varrho_{*i}^{2/3}$ , could be satisfied with significantly smaller applied RMP relative amplitudes  $B_{mn}^{\text{vac}}/B_{t0} \propto \rho_{*i}^{4/3}$  than that in DIII-D discharge 158115 [14, 15].

*Relation to RMP blockage of pedestal width growth* [53]. A more recent, foresightful and related model for RMP ELM suppression is based on an empirically-based phenomenological model of the effects of RMPs on the growth of pedestal widths in DIII-D [53]. That model proposes that “a ‘wall’ associated with the RMP blocks the inward penetration of the edge transport barrier.” In its significant RMP penetration at the pedestal top causes an RMP-induced magnetic island or region of strong RMP-induced transport there which prevents the radial expansion of the pedestal to an unstable width for P-B modes. In the model developed here for DIII-D discharge 158115 [14, 15] the focus is on the dynamics of how an ELM crash induces sufficient magnetic reconnection which eventually produces a slowly growing magnetic island width and resultant flutter-induced transport that reduces the radial gradients of  $T_e$  and  $n_e$  at the pedestal top to the level observed during ELM suppression. Thus, the present model could be viewed as developing a quantifiable framework for how RMPs produce an ELM-crash-induced dynamical evolution into ELM suppression whose effects are somewhat analogous to those in the empirical RMP pedestal width growth blockage model [53].

## 11. Summary

*Conclusions.* A comprehensive model has been developed to describe and quantify the physical processes involved in the many stages of  $n = 2$  RMP effects near threshold conditions and an ELM crash response that lead to bifurcation into an ELM-suppressed state in DIII-D discharge 158115 [14, 15]: 1) in the ELMing equilibrium before suppression of ELMs, flow screening of RMPs is strong at  $q = m/n$  rational surfaces with little magnetic reconnection there; 2) an ELM crash produces an abrupt, large amount of forced magnetic reconnection at rational surfaces; 3) this large ELM-crash-induced magnetic perturbation at the 8/2 rational surface forces the radial electric field to zero there and thus locks the toroidal flow there to the stationary RMP frame (like field-error-induced mode locking); 4) this tearing-type magnetic perturbation also provides an 8/2 seed magnetic island (like for NTMs) that is governed by the modified Rutherford equation in (17); 5) then, if the applied 8/2 RMP is large enough to satisfy (18), the response bifurcates into a growing 8/2 magnetic island [see Fig. 6(c)]; and 6) the RMPs produce magnetic-flutter-induced electron density and temperature diffusivities that are at levels observed in the ELM suppressed state where P-B modes are stabilized.

*RMP ELM suppression criteria.* As discussed in the preceding section, the key criteria for obtaining RMP ELM suppression in this new model are: 1) an ELM crash must induce enough magnetic field reconnection at the top of a pedestal to provide a large enough seed island and lock the magnetic perturbation to the stationary RMP frame, and 2) the externally applied RMP at the 8/2 surface must be large enough for its effects to dominate in the nonlinear modified Rutherford equation, as specified in (18), and the flutter transport it induces must be large enough to suppress P-B modes.

*Some caveats.* The various predictions of the comprehensive model developed in this paper agree with many experimental results to within a factor of two or less for DIII-D discharge 158115 [14, 15]. However, unknown parameters in some of the phenomenological models have been chosen in order to illustrate the possible magnitudes of various parameters and so all the numbers work out reasonably well. Also, many of the theory-based models are approximate or sometimes extended somewhat outside their rigorously derived regimes of validity. Further, more and more detailed data and analyses are needed, especially during and just after the ELM crash that precedes ELM suppression, to definitively test many of the key elements of this near threshold model for ELM suppression. Further, much research remains to extend and hopefully validate this model of ELM-crash-induced RMP ELM suppression for different RMP spectra, electron flows and collisionalities at key rational surfaces etc.

*Model extrapolation.* It is important to emphasize that the analysis in this paper is for discharge 158115 in DIII-D [14, 15]. More work is needed to determine how universal this ELM-crash-induced RMP ELM suppression model is and its usefulness for developing criteria for achieving ELM suppression in other RMP experiments in DIII-D and other tokamaks. Of particular interest would be tests of the  $w_{\text{vac}}^{\text{crit}} \propto \rho_{*i}^{2/3}$  scaling in (18) and thus the scaling of the needed  $B_{mn}^{\text{vac}}/B_{t0}$  with  $\rho_{*i}^{4/3}$ , which is encouraging for ITER.

## Acknowledgments

The authors are grateful to T.E. Evans, M.E. Fenstermacher and R.A. Moyer for many useful discussions about their pioneering use of RMPs for ELM suppression in DIII-D. The first author is grateful to R.A. Moyer for highlighting the possible importance of ELM crashes in initiating ELM suppression, R.J. Groebner for useful discussions, and S.P. Smith and L. Cui for preliminary studies of flutter transport in discharge 158115.

This material is based on work supported by the U.S. Department of Energy, Office of Science, Office of Fusion Energy Sciences under Award Numbers DE-FG02-92ER54139, DE-FG02-86ER53218, DE-AC02-09CH11466 and DE-FC02-04ER54698. DIII-D data shown in this paper can be obtained in digital format by following the links at [https://fusion.gat.com/global/D3D\\_DMP](https://fusion.gat.com/global/D3D_DMP). — to be provided later.

- [1] Loarte A *et al* 2003 *Plasma Phys. Control. Fusion* **45** 1549
- [2] Evans T E *et al* 2004 *Phys. Rev. Lett.* **92** 235003
- [3] Moyer R A *et al* 2005 *Phys. Plasmas* **12** 056119
- [4] Evans T E *et al* 2006 *Nature Phys.* **2** 419
- [5] Evans T E *et al* 2008 *Nucl. Fusion* **48** 024002
- [6] Hegna C C, Connor J W, Hastie R J and Wilson H R 1996 *Phys. Plasmas* **3** 584
- [7] Connor J W, Hastie R J, Wilson H R and Miller R L 1998 *Phys. Plasmas* **5** 2687
- [8] Wilson H R, Snyder P B, Huysmans G T A and Miller R L 2002 *Phys. Plasmas* **9** 1277
- [9] Snyder P B, Wilson H R, Ferron J R, Lao L L, Leonard A W, Osborne T H, Turnbull A D, Mossessian D, Murakami M and Xu X Q 2002 *Phys. Plasmas* **9** 2037
- [10] Zohm H 1996 *Plasma Phys. Control. Fusion* **38** 105
- [11] Suttrop W 2000 *Plasma Phys. Control. Fusion* **42** A1
- [12] Callen J D 2011 *Nucl. Fusion* **51** 094026
- [13] Joseph I 2012 *Contrib. Plasma Phys.* **52** 326
- [14] Paz-Soldan C *et al* 2015 *Phys. Rev. Lett.* **114** 105001
- [15] Nazikian R *et al* 2015 *Phys. Rev. Lett.* **114** 105002
- [16] Fitzpatrick R 1993 *Nucl. Fusion* **33** 1049
- [17] Fitzpatrick R 1998 *Phys. Plasmas* **5** 3325
- [18] Hahm T S and Kulsrud R M 1985 *Phys. Fluids* **28** 2412
- [19] Waelbroeck F L 2003 *Phys. Plasmas* **10** 4040
- [20] Cole A J and Fitzpatrick R 2006 *Phys. Plasmas* **13** 032503
- [21] Heyn M F, Ivanov I B, Kasilov S V, Kernbichler W, Joseph I, Moyer R A and Runov A M 2008 *Nucl. Fusion* **48** 024005
- [22] Nardon E, Tamain P, Bécoulet M, Huysmans G and Waelbroeck F L 2010 *Nucl. Fusion* **50** 034002
- [23] Waelbroeck F L, Joseph I, Nardon E, Bécoulet M and Fitzpatrick R 2012 *Nucl. Fusion* **52** 074004
- [24] Callen J D, Hegna C C, and Beidler M 2016 “Forced magnetic reconnection in tokamak plasmas,” to be published.
- [25] Ferraro N M 2012 *Phys. Plasmas* **19** 056105
- [26] Callen J D, Groebner R J, Osborne T H, Canik J M, Owen L W, Pankin A Y, Rognlén T D and Stacey W M 2010 *Nucl. Fusion* **50** 064004
- [27] Callen J D 1977 *Phys. Rev. Lett.* **39** 1540
- [28] Callen J D, Cole A J and Hegna C C 2012 *Phys. Plasmas* **19** 112505
- [29] Callen J D, Hegna C C and Cole A J 2013 *Nucl. Fusion* **53** 113015
- [30] Rutherford P H 1973 *Phys. Fluids* **16** 1903
- [31] Furth H P, Killeen J and Rosenbluth M N 1963 *Phys. Fluids* **6** 459
- [32] Hegna C C and Callen J D 1994 *Phys. Plasmas* **1** 2308

- [33] Ren C, Callen J D, Gianakon T A, Hegna C C, Chang Z, Fredrickson E D, McGuire K M, Taylor G, and Zarnstorff M C 1998 *Phys. Plasmas* **5** 450
- [34] Braginskii S I 1965 “Transport processes in a plasma,” in *Reviews of Plasma Physics*, Editor Leontovich M A (Consultants Bureau, New York, 1965) Vol. I p 205
- [35] Gohil P, Burrell K H, Groebner R J, Kim J, Martin W C, McKee E L and Seraydarian R P 1991 *Proc. 14th Symp. in Fusion Engineering (San Diego, CA)* vol 2 (New York: Institute of Electrical and Electronics Engineers) p 1199
- [36] Chrystal C, Burrell K H, Grierson B A, Haskey S R, Groebner R J, Kaplan D H, and Briesemeister A 2016 *Rev. Sci. Instrum.* **87**, 11E512 (2016)
- [37] Heyn M E, Ivanov I B, Kasilov S V, Kernbichler W, Lettner P, Nemov V V, Suttrop W and the ASDEX Upgrade Team 2014 *Nucl. Fusion* **54** 064005
- [38] Hegna C C, Callen J D and LaHaye R J 1999 *Phys. Plasmas* **6** 130
- [39] Chang Z, Callen J D, Fredrickson E D, Budny R V, Hegna C C, McGuire K M, Zarnstorff M C and TFTR group 1995 *Phys. Rev. Lett.* **74** 4663
- [40] La Haye R J 2006 *Phys. Plasmas* **13** 055501
- [41] Zhu P, Hegna C C, Sovinec C R 2009 *Phys. Rev. Lett.* **102** 235003
- [42] Callen J D, Cole A J and Hegna C C 2009 *Phys. Plasmas* **16** 082504; 2013 Erratum **20** 069901
- [43] Hirshman S P 1978 *Nucl. Fusion* **18** 917
- [44] Smolyakov A I, Hirose A, Lazzaro E, Re G B, Callen J D 1995 *Phys. Plasmas* **2** 1581
- [45] Wilson H, Connor J W, Hastie R J and Hegna C C 1996 *Phys. Plasmas* **3** 248
- [46] Qu H, Peng X, Wang F, Wang A, and Shen Y 2016 *Phys. Plasmas* **23** 092511
- [47] See Fig. 3(b) in La Haye R J, Prater R, Buttery R J, Hayashi N, Isayama A, Maraschek M E, Urso L and Zohm H 2006 *Nucl. Fusion* **46** 451
- [48] La Haye R.J. *et al* 2014 “Insights Into  $m/n=2/1$  Tearing Mode Stability Based on Initial Island Growth Rate in DIII-D ITER Baseline Scenario Discharges” at 41<sup>st</sup> EPS Conference on Plasma Physics, Berlin, Germany, June 23–27 (to be submitted to *Plasma Phys. Control. Fusion* )
- [49] La Haye R J 2015 “A Fresh Look at Electron Cyclotron Current Drive Power Requirements for Stabilization of Tearing Modes in ITER” paper I15 at 21st Topical Conference on Radiofrequency Power in Plasmas, UCLA Conference Center at Lake Arrowhead, California, April 27–29
- [50] Fitzpatrick R 2005 *Phys. Plasmas* **2** 825
- [51] Raum P T, Smith S P, Callen J D, Ferraro N M, and Meneghini O 2015 “Modeling of magnetic flutter-induced transport in DIII-D,” report GA-A27559.
- [52] Callen J D 2014 *Contrib. Plasma Phys.* **54** 484
- [53] Snyder P B, Osborne T H, Burrell K H, Groebner R J, Leonard A W, Nazikian R, Orlov D M, Schmitz O, Wade M R, and Wilson H R 2012 *Phys. Plasmas* **19** 056115
- [54] Fenstermacher M E *et al* 2008 *Phys. Plasmas* **15** 056122
- [55] Schmitz O *et al* 2009 *Phys. Rev. Lett.* **103** 165005
- [56] Schmitz O *et al* 2012 *Nucl. Fusion* **52** 043005
- [57] Rechester A B and Rosenbluth 1978 *Phys. Rev. Lett.* **40** 38